North Atlantic Ocean-Originated Multicentennial Oscillation of the AMOC: A Coupled Model Study

Kunpeng Yang,[a] Haijun Yang,*[a] Yang Li,[b] and Qiong Zhang[c]

[a] *Department of Atmospheric and Oceanic Sciences and Key Laboratory of Polar Atmosphere-ocean-ice System for Weather and Climate of Ministry of Education, Fudan University, Shanghai, 200438, China*

[b] *Department of Atmospheric and Oceanic Sciences, School of Physics, Peking University, Beijing, 100871, China*

[c] *Department of Physical Geography and Bolin Centre for Climate Research, Stockholm University, Stockholm, 10691, Sweden*

Journal of Climate

1st submission, July 13, 2023

1st revision, October 30, 2023

Corresponding author: Haijun Yang, yanghj@fudan.edu.cn

ABSTRACT

A multicentennial oscillation (MCO) of the Atlantic meridional overturning circulation (AMOC) is exhibited in a CESM1 control simulation. It primarily arises from internal oceanic processes in the North Atlantic, potentially representing a North Atlantic Ocean-originated mode of AMOC multicentennial variability (MCV) in reality. Specifically, this AMOC MCO is mainly driven by salinity variation in the subpolar upper North Atlantic, which dominates local density variation. Salinity anomaly in the subpolar upper ocean is enhanced by the well-known positive salinity advection feedback that is realized through anomalous advection in the subtropical-subpolar upper ocean. Meanwhile, northward advection of salinity anomaly from the subtropical intermediate ocean through mean advection weakens the salinity anomaly in the subpolar upper ocean, leading to its phase change. This mechanism aligns with a theoretical model we proposed earlier. In this theoretical model, artificially deactivating either the anomalous or mean advection in the AMOC upper branch prevents it from exhibiting AMOC MCO, underscoring the indispensability of both the anomalous and mean advections in this North Atlantic Ocean-originated AMOC MCO. In our coupled model simulation, the South Atlantic and Southern Ocean do not exhibit variabilities synchronous with the AMOC MCO; the Arctic Ocean’s contribution to the subpolar salinity anomaly is much weaker than the North Atlantic. Hence, this North Atlantic Ocean-originated AMOC MCO is distinct from the previously proposed Southern Ocean-originated and Arctic Ocean-originated AMOC MCOs.

KEYWORDS: Coupled model, Atlantic meridional overturning circulation, Multicentennial oscillation, Salinity anomaly

1. Introduction

Paleoclimatic proxy data from various sources reveal multicentennial variability (MCV) of the Earth's climate system (Chapman and Shackleton 2000; Nyberg et al. 2002; Kim et al. 2004; Wanner et al. 2008; Newby et al. 2014; Askjær et al. 2022), yet its origin and underlying mechanism remain elusive. The Atlantic meridional overturning circulation (AMOC), a crucial regulator of the climate system, also displays variability on this multicentennial timescale (Kissel et al. 2013; Thornalley et al. 2013). Consequently, MCV of the AMOC has been proposed as a potential driver of the climate system's MCV (McDermott et al. 2001; Oppo et al. 2003; Hall et al. 2004; Miettinen et al. 2012; Chabaud et al. 2014; Ayache et al. 2018; Thirumalai et al. 2018).

Due to the scarcity of long-term direct AMOC observations, research on AMOC MCV has primarily relied on models of a hierarchy of complexities. Early studies have identified AMOC MCVs in two-dimensional (Mysak et al. 1993) and three-dimensional (Mikolajewicz and Maier-Reimer 1990; Winton and Sarachik 1993; Drijfhout et al. 1996) ocean models. Over the past two decades, several studies have utilized the more sophisticated coupled models to study AMOC MCV (Park and Latif 2008; Delworth and Zeng 2012; Martin et al. 2013, 2015; Jiang et al. 2021; Meccia et al. 2023). Perhaps because of the differences in models employed, the mechanisms underlying these coupled model AMOC MCVs vary. Consequently, these studies might have identified distinct potential modes of the real-world AMOC MCV, which do not necessarily contradict each other. Hence, it might be more suitable to refer to the MCVs of AMOC in these studies as MCOs, as the term "variability" is usually from an observational or statistical view, but "oscillation" is often dominated by a specific dynamic mode and carries a more physical connotation (Liu 2012; Sutton et al. 2018; Zhang et al. 2019). In this context, studying the AMOC MCV essentially involves tackling a dynamic system problem, that is, a comprehensive understanding of the real-world AMOC MCV critically depends on understanding each constituent mode (or AMOC MCO). Analyses of the modeled AMOC MCOs, therefore, should draw insights from the more fundamental (and typically earlier) theoretical studies. However, these coupled model studies often do not interpret their AMOC MCOs from a more theoretical and dynamic perspective, highlighting a disconnect between model results and theories.

Unlike the El Niño-Southern Oscillation, where both linear (Suarez and Schopf 1988; Jin 1997) and nonlinear theories (Tziperman et al. 1994; Sun 1997) have been extensively developed, the majority of low-frequency AMOC oscillation theories focus on linear oscillation (Griffies and

Tziperman 1995; Rivin and Tziperman 1997; Wei and Zhang 2022), where the AMOC oscillation is regular and symmetric. Under the linear framework, the single-equilibrium oscillation is perceived as an anomaly hovering around the unstable equilibrium. Positive and negative feedbacks enhance and weaken the anomaly, collectively leading to the anomaly's phase transition and therefore its cyclic evolution. This forms our foundational "theoretical interpretation" of linear oscillation, by which we are inspired to review the aforementioned coupled model studies on AMOC MCO.

In an earlier study using the Kiel Climate Model (KCM), Park and Latif (2008) found an AMOC oscillation with a period of 300-400 years. Their follow-up studies, Martin et al. (2013, 2015) proposed that this AMOC MCO originates from the Southern Ocean. When the AMOC is anomalously strong, heat content of the mid-depth water in the Weddell Sea increases due to strengthened southward transport of the warmer North Atlantic Deep Water (NADW). Deep convection in the Southern Ocean is triggered when the mid-depth heat accumulation becomes excessive, hence the warm deeper water reaches the cold surface air and convectively releases heat to the atmosphere, densifying the Weddell Sea overall. Therefore, the Atlantic north-to-south density gradient is decreased, limiting the NADW formation and thus the AMOC strength (Hughes and Weaver 1994). This is similar to the advective-convective mechanism proposed by Yin (1995), where convection is initiated by the advective buildup of heat. Therefore, the oscillation timescale is set by the advective heat accumulation. Yet, this AMOC MCO is induced by the drastic "flip-flop" convection (Welander 1982) in the Southern Ocean, which is in essence a multi-equilibrium phenomenon.

Using a GFDL CM2.1 model simulation, Delworth and Zeng (2012) also identified an AMOC MCO related to the Southern Ocean, but with a different mechanism. Starting with a weak AMOC, a positive surface salinity anomaly in the Southern Ocean is carried northward by the mean circulations in the upper branch of the AMOC, strengthening the NADW formation when it reaches the North Atlantic convection region, driving the AMOC into its positive phase. Synchronously, more freshwater is produced in the Southern Ocean due to the positive AMOC anomaly, and would be transported northward later. This will weaken the AMOC when the negative salinity anomaly reaches the northern convection region, completing a full cycle. The oscillation timescale here is determined by the time consumed in transporting the Southern Ocean salinity anomaly to the North Atlantic; no drastic variation of deep convection in the Southern Ocean is documented by the authors. Therefore, it is a Southern Ocean-originated AMOC MCO whose essence differs from the "flip-flop" AMOC

MCO in Park and Latif (2008). In short, the mean advection process is raised as the driver for the entire cycle, including the growing and weakening of the anomalies, as well as the phase transition. However, considering that the mean advection process is a weakening process for salinity anomaly in the subpolar North Atlantic (Griffies and Tziperman 1995; Wei and Zhang 2022), there should be processes that enhance the subpolar salinity anomaly, which are not resolved in this study.

Recently, a group of studies identified Arctic Ocean-originated AMOC MCOs. Jiang et al. (2021) found a 200-year AMOC MCO in their IPSL-CM6A-LR model simulation. When the AMOC resides in its strong phase, the Arctic Ocean is warmed and thus more sea ice melting leads to negative salinity anomaly therein. The negative Arctic Ocean salinity anomaly is advected southward through mean advection, inhibiting the subpolar deep convection and driving the AMOC into its negative phase. Meccia et al. (2023) found a 150-year AMOC oscillation in the EC-Earth3 model with a similar mechanism. Resemblance in explanations proposed by these two studies might be attributed to the shared ocean component (NEMO 3.6) of their models. As with Delworth and Zeng (2012), the mean advection is again proposed as the process governing the entire evolution, suggesting that enhancing processes for the AMOC anomaly remain to be found. Another study by Mehling et al. (2023) also proposed salinity anomaly from the Arctic Ocean as the driver for their modeled AMOC MCO, but they utilized an intermediate-complexity model instead of a high-complexity coupled model. In addition, Vellinga and Wu (2004) analyzed an AMOC oscillation on centennial instead of multicentennial timescale, with the air-sea interaction rather than internal oceanic processes as the core mechanism. As such, we have not included Vellinga and Wu (2004) and Mehling et al. (2023) in coupled model AMOC MCO studies.

The ability to test whether these aforementioned AMOC MCOs exist in reality is constrained by observational limitations. Therefore, interpreting coupled model AMOC MCOs from a more fundamental and theoretical perspective is a practical approach to improve the understanding of the real-world AMOC MCV at this stage. By analyzing results from a CESM1 control simulation, we identified an AMOC MCO dominated mainly by processes in the North Atlantic. Its mechanism can be explained by a linear AMOC MCO theory we proposed earlier in Li and Yang (2022) (hereafter LY22). The theoretical box model in LY22 is inspired by another theoretical box model proposed by Griffies and Tziperman (1995) (hereafter GT95), which focuses on AMOC multidecadal oscillation. Both theoretical models only include processes in the North Atlantic, and are therefore unable to exhibit AMOC oscillations related to other ocean basins. In the GT95 theoretical model, the depth of the upper boxes is set at only 300 m. In addition, the volume of the subpolar boxes is set to only 1/11 of the North Atlantic, which is too small as the latitude for deep water formation (DWF) spans from approximately 50°N to 75°N (Hansen et al. 2003; Kieke and Yashayaev 2015). LY22 adopted new model parameters including thicker upper boxes and larger subpolar boxes, and found that the model exhibits AMOC MCO. By including a nonlinear subpolar vertical mixing into the purely linear advection system, a self-sustained AMOC oscillation is realized in LY22. By contrast, GT95 focused on stochastically-forced oscillation and the AMOC multidecadal oscillation therein is a damped oscillation. In LY22, the AMOC anomaly is enhanced by the positive salinity advection feedback in the upper level of the subtropical-subpolar North Atlantic, and weakened by the mean advection of salinity anomaly in the upper ocean. Starting with a positive AMOC anomaly, more subtropical saline water is transported northward, further strengthening the AMOC anomaly. This constitutes the classical positive salinity advection feedback (Stommel 1961; Marotzke 1996). On the other hand, a negative salinity anomaly formed in the subtropical upper ocean is transported northward through mean advection, weakening the AMOC anomaly.

In this study, we will treat the AMOC MCO in the CESM1 control simulation as a linear oscillation, and analyze its mechanism in a linear framework. In section 2, an approach for extracting low-frequency variability from the raw model data is introduced. In section 3, the MCOs of the AMOC and global buoyancy fields are presented; dominance of salinity variation in the AMOC MCO is highlighted. In section 4, the evolution patterns of salinity anomalies are shown. In section 5, processes contributing to the AMOC MCO are quantitatively analyzed, and the significance of the key advection processes is examined employing the theoretical model in LY22. In section 6, the conclusion and discussion are provided.

2. Model and methods

a. Pre-industrial control simulation

The coupled model employed is the Community Earth System Model (CESM, version 1.0.4) developed by the National Centre for Atmospheric Research (NCAR). It is a global climate model consisting of five components: atmosphere, land surface, ocean, sea ice, and ice sheet (not active). A coupler exchanges data between these components.

The model grid utilized is f19_gx1v6. The atmospheric component is the Community Atmosphere Model version 4 (CAM4) (Neale et al. 2010), with 26 vertical levels and a horizontal resolution of 1.9° × 2.5°. The land surface model is the Community Land Model version 4 (CLM4) (Lawrence et al. 2011), with the same horizontal resolution as CAM4. The ocean model is the Parallel Ocean Program version 2 (POP2) (Smith et al. 2010). It uses the gx1v6 curvilinear grid, having 384 × 320 grid points horizontally and 60 layers vertically. The horizontal grid is zonally uniform at a 1.125° resolution but meridionally non-uniform, with a 0.27° resolution near the equator, increasing to 0.65° at 60°N/S and then decreasing toward the polar regions. The sea ice model is the Community Ice Code (CICE4) (Hunke and Lipscomb 2010), with the same horizontal resolution as POP2. The coupler is the CESM Coupler CPL7 (Craig et al. 2012).

In the ocean model, velocity is divided into three components: explicit Eulerian-mean velocity, parameterized bolus velocity, and parameterized sub-mesoscale velocity (Gent and McWilliams 1990; Fox-Kemper and Ferrari 2008; Fox-Kemper et al. 2008); the latter two are collectively regarded as the parameterized eddy-induced velocity. These three velocity components have their corresponding transport or streamfunction. The total, or referred to as "residual," velocity (streamfunction) is the sum of these three components. A 2500-year control simulation is conducted from the rest with pre-industrial configuration, to assure that the thermohaline circulation has reached its equilibrium before our study period. In this study, outputs of the last 1500 years are analyzed.

b. Data analysis methods

Instead of using the traditional empirical orthogonal function (EOF) method, the low-frequency component analysis (LFCA) method (Wills et al. 2018) is adopted to evaluate the low-frequency AMOC variability. The LFCA provides linear combinations of the first n EOFs and principal components (PCs) of the data. The results are n low-frequency patterns (LFPs) as the spatial patterns and n corresponding low-frequency components (LFCs) as the time series. The LFPs and corresponding LFCs are ranked in a descending order according to the ratio of their low-frequency variances (obtained through a low-pass filter) to the total variance of the first n EOFs. Therefore, low-frequency signals are the most concentrated in LFP1 and LFC1, which are our focus. More details about the LFCA method can be found in Wills et al. (2018). As demonstrated in Jiang et al. (2021), the LFCA outperforms the EOF method in extracting and analyzing low-frequency variability of the AMOC.

A Lanczos filter with 121 weights and 60 years cut-off period is used for the LFCA and for filtering other time series throughout this study. Power spectral analysis is conducted for both the unfiltered AMOC index and AMOC LFC1. Significance at 95% confidence level and the best-fit first-order Markov red noise spectrum are presented along with the power spectrum.

To quantify the contributions to salinity anomaly of a specific region from different processes, liquid freshwater mass transport (kg s^{-1}) into the region is computed. The total liquid freshwater mass transports across the x-direction and y-direction of the ocean model grids are computed as:

$$F_x = \int_{y_s}^{y_n} \int_{z_b}^{z_t} (1 - \frac{S}{S_{ref}}) \rho u dz dy \tag{1}$$

$$F_y = \int_{x_w}^{x_e} \int_{z_b}^{z_t} (1 - \frac{S}{S_{ref}}) \rho v dz dx \tag{2}$$

, respectively. The anomaly of advection-induced liquid freshwater mass transport can be linearly decomposed into three components: (1) anomalous advection of mean salinity induced; (2) mean advection of salinity anomaly induced; and (3) anomalous advection of salinity anomaly induced. The third component is a nonlinear advection term that is much smaller than the former two components, hence is disregarded. The liquid freshwater mass transports induced by anomalous advection of mean salinity are expressed as $\int_{y_s}^{y_n} \int_{z_b}^{z_t} (1 - \frac{\overline{S}}{S_{ref}}) \rho u' dz dy$ and $\int_{x_w}^{x_e} \int_{z_b}^{z_t} (1 - \frac{\overline{S}}{S_{ref}}) \rho v' dz dx$; the liquid freshwater mass transports induced by mean advection of salinity anomaly are expressed as $\int_{y_s}^{y_n} \int_{z_b}^{z_t} - \frac{S'}{S_{ref}} \rho \overline{u} dz dy$ and $\int_{x_w}^{x_e} \int_{z_b}^{z_t} - \frac{S'}{S_{ref}} \rho \overline{v} dz dx$. y_s, y_n, x_w, and x_e are the southernmost, northernmost, westernmost, and easternmost grid points. z_b and z_t are the bottommost and uppermost grid points. S, $\overline{S}$, and S' are the three-dimensional sea water salinity in psu, its climatological value, and its anomaly. S_{ref} is the reference sea water salinity of the given study area. ρ is the sea water density in kg m^{-3}. u, $\overline{u}$, and u' (v, $\overline{v}$, and v') are the three-dimensional x-direction (y-direction) velocity in m s^{-1}, its climatological value, and its anomaly.

3. MCOs in the coupled model

a. AMOC

The modeled AMOC index exhibits a distinct MCV (Fig. 1a), with the most significant peak around 375 years (Fig. 1b). The AMOC index is defined as the maximum total meridional streamfunction within the North Atlantic region spanning 20°-70°N and 200-3000 m. The AMOC index exhibits a stable oscillation around its mean state, with a magnitude of around 2 Sv, about 10% of the climatological value (24 Sv). As we will interpret the modeled AMOC MCV as a linear oscillation, henceforth the MCVs of the AMOC and other variables will be referred to as MCOs. The climatological AMOC exhibits an overall northward branch in the upper 0-1000 m, a deep convection branch around 60°N, and a southward NADW branch in the deep ocean of 1500-3000 m (Fig. 1e). The maximum value is located near 1000 m at around 40°N.

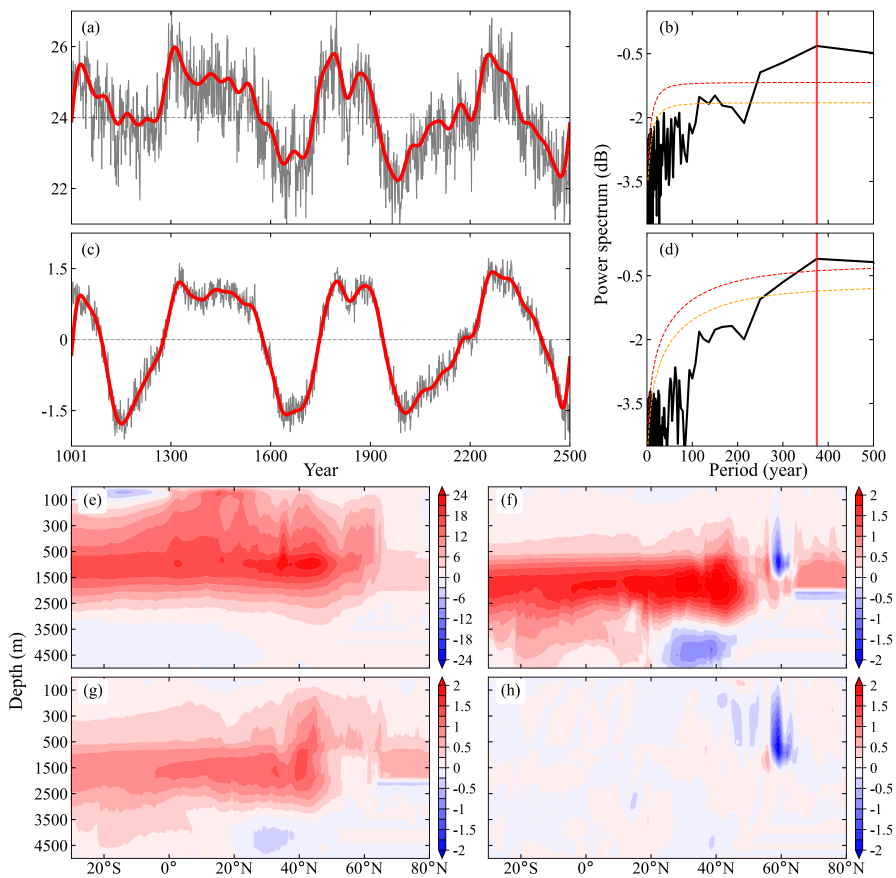

FIG. 1. (a) Time series for the Atlantic meridional overturning circulation (AMOC) index (units: Sv; 1 Sv = 10^6 m^3 s^{-1}) of model years 1001-2500. The AMOC index is defined as the maximum total meridional streamfunction in the North Atlantic spanning 20°-70°N and 200-3000 m. The gray curve represents the unfiltered AMOC index, and the red curve is the low-pass-filtered AMOC index using the Lanczos filter. The horizontal dashed line denotes the climatological value of the AMOC (24 Sv). (b) Power spectrum (units: dB) of the unfiltered AMOC index, with period as the abscissa. The dashed orange and red curves represent the best-fit first-order Markov red noise spectrum and the significance at 95% confidence level, respectively. The vertical red line denotes the most significant peak (375 years). (c) Same as (a), but for the AMOC's first low-frequency component (LFC1). Before applying the low-frequency component analysis (LFCA) method, the data is detrended and then weighted according to the square root of grid cell thicknesses. The Lanczos filter is used for the LFCA. (d) Same as (b), but for the AMOC LFC1. (e) Climatological pattern of the total AMOC averaged over years 1001-2500 (units: Sv). (f) Pattern of the AMOC's first low-frequency pattern (LFP1) (units: Sv). (g) and (h) are the regression patterns of the Eulerian-mean and eddy-induced AMOCs on the AMOC LFC1 (units: Sv), respectively.

To better depict the low-frequency variability of the AMOC, the LFCA method is applied to the total AMOC. The first 10 EOFs are utilized, which explain 93.7% of the total variance. High-frequency signals of the AMOC are substantially weakened in the AMOC LFC1 (Figs. 1c, d). The power spectrum of the AMOC LFC1 reveals that the most significant peak persists near 375 years and becomes the only peak passing the significance test (Fig. 1d). The AMOC LFP1 accounts for 87.5% of the low-frequency variance of the first 10 EOFs. The pattern of the AMOC LFP1 (Fig. 1f) aligns with that of the climatological AMOC (Fig. 1e), but exhibits a structure with negligible transport above 500 m. The upper ocean wind-driven subtropical cell, which is discernible in the climatological AMOC pattern (Fig. 1e), has been filtered out in the AMOC LFP1 (Fig. 1f). This suggests that the AMOC MCO in this study primarily occurs in the lower ocean, and the high-frequency variability that may be related to the upper ocean wind-driven circulation should be ruled out.

The Eulerian-mean component of the AMOC demonstrates a coherent meridional variability throughout the Atlantic basin (Fig. 1g), while the eddy-induced component has a significant local variability within the subpolar North Atlantic (Fig. 1h). The fluctuation of the eddy-induced AMOC is of comparable magnitude to that of the Eulerian-mean AMOC, but with an opposite sign in the subpolar deep convection region, resulting in the negative signal at the same position of the AMOC LFP1 (Fig. 1f). This suggests that a stronger (weaker) Eulerian-mean AMOC is associated with a weaker (stronger) eddy-induced AMOC. Although the causality between the Eulerian-mean and eddy-induced AMOCs in the current study is not yet clear, Figs. 1f and 1h suggest that the eddy-induced AMOC plays a role in this AMOC MCO.

b. Global surface buoyancy fields

Consistent with the AMOC LFC1, the global ocean's surface buoyancy fields also exhibit remarkable MCOs (Fig. 2). The LFCA is conducted for the global sea surface density (SSD) anomaly, SSD anomaly induced by sea surface salinity (SSS) anomaly, and SSD anomaly induced by sea surface temperature (SST) anomaly according to Roquet et al. (2015). All of their LFC1s reflect variability on multicentennial timescale (Fig. 2a).

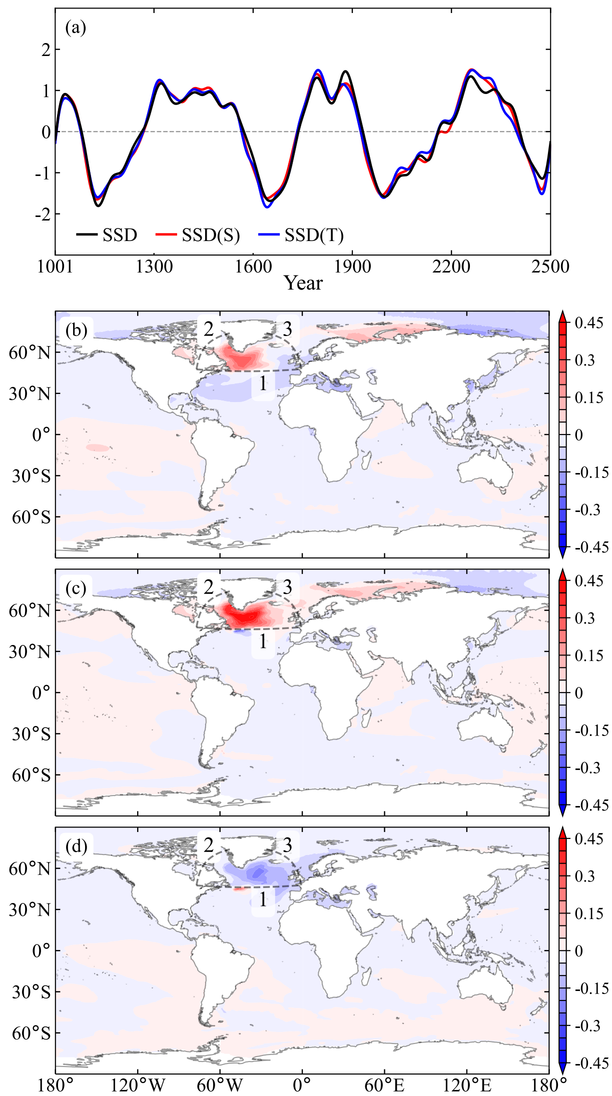

FIG. 2. (a) Filtered LFC1s (units: dimensionless) of the global sea surface density (SSD) anomaly (black curve), SSD anomaly induced by sea surface salinity (SSS) anomaly (red curve), and SSD anomaly induced by sea surface temperature (SST) anomaly (blue curve). (b) LFP1 (units: kg m^{-3}) of the global SSD anomaly. (c) and (d) are the same as (b), but for the SSD anomalies induced by SSS and SST anomalies, respectively. Before the LFCA, the data is detrended and then weighted according to the square root of grid cell areas. The Lanczos filter is applied in (a); and the LFCA, in (b)-(d). The region enclosed by boundaries 1-3 (dashed curves in Figs. 2b-d) represents the deep water formation (DWF) region, and will be used later. These boundaries are parallel to the grid lines of the ocean model. Boundary 1 is along 47°N.

The LFP1s of the global surface buoyancy fields indicate that the strongest multicentennial signals are located in the North Atlantic (Figs. 2b-d), especially in the DWF region in the subpolar North Atlantic with the deepest March mixed layer depth simulated (figure not shown). These spatial patterns indicate that in both the North Atlantic and Arctic Ocean, the SSD anomalies (Fig. 2b) are dominated by SSS anomalies (Fig. 2c), yet partly canceled by SST anomalies (Fig. 2d). Over the "transition zone" near 45°N along the Gulf Stream extension (Buckley and Marshall 2016), the local density variability is negligible (Fig. 2b) due to the counteractive effects from anomalous salinity and temperature. Multicentennial signals in the other basins, such as the South Atlantic, Southern Ocean, and the Pacific and Indian Oceans, are rather weak. In this study, the DWF region is defined as the region enclosed by boundaries 1-3 (Figs. 2b-d); boundary 1 is situated just to the "transition zone."

4. Evolution of salinity anomalies in the Atlantic

a. Latitude-depth patterns

We first examine the model distribution of climatological salinity in the Atlantic (Fig. 3). In the North Atlantic, the meridional gradient of climatological salinity is generally greater in the upper ocean and decreases with depth. Specifically, the most saline water (salinity higher than 36.5 psu) is located in the subtropical upper ocean between 20°N and 40°N, extending downward to 1500 m and then southward to 40°S in the deep ocean. The more saline subtropical water is separated from the fresher subpolar water by the Gulf Stream extension and the North Atlantic Current (NAC), forming the subpolar front near 45°N, whose location is consistent with the downward branch of the AMOC (Fig. 1e). The more saline subtropical water also extends northward to the subpolar subsurface ocean, against the freshwater from the Arctic Ocean. On the other hand, fresher water (salinity lower than 34 psu) comes mainly from the surface of the subpolar Southern Ocean, extending downward and northward and occupying the southern subtropical ocean between 200 m and 1500 m, forming the Antarctic Intermediate water.

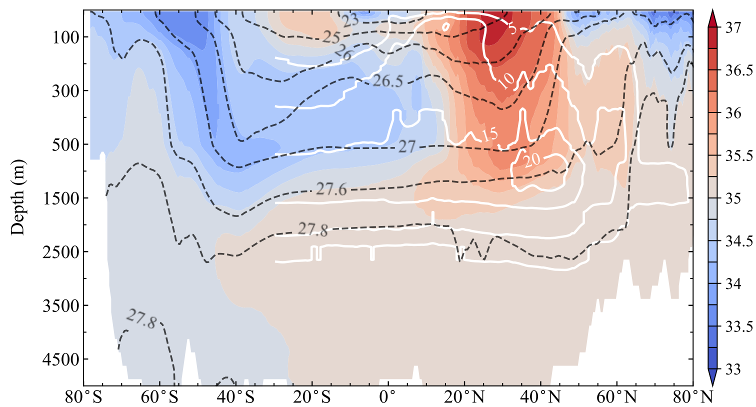

FIG. 3. Climatological salinity zonally averaged in the Atlantic (shading; units: psu), superimposed with climatological potential density (σ_θ) (black contour; units: kg m^{-3}) and AMOC (white contour; units: Sv).

Next, evolution of salinity anomalies with the AMOC over the multicentennial cycle is analyzed. Figure 4 illustrates the lead/lag regression coefficients of the zonally averaged salinity anomalies in the Atlantic on the AMOC LFC1, superimposed with climatological potential density (σ_θ). Positive and negative regression coefficients at lag n years represent that generally there are positive and negative salinity anomalies in the corresponding regions, respectively, when salinity anomalies lag the AMOC LFC1 by n years. For conciseness, positive/negative salinity anomaly is used to represent positive/negative regression coefficient, which can be rough to some extent.

When the salinity anomalies lead the AMOC LFC1 by 200 years (Fig. 4a), there is a pronounced negative salinity anomaly centered in the upper ocean around 55°N, corresponding to the weakest NADW formation and AMOC. This negative anomaly extends from the surface to deep ocean of the North Atlantic north of 45°N, and occupies 1500-3500 m in the deep ocean south of 45°N. South of the subpolar negative anomalies, broad positive anomalies are observed at lower latitudes, occupying the upper 1500 m of the Atlantic. The negative anomalies are the strongest in the upper DWF region, while the positive anomalies have the greatest magnitude in the subtropical intermediate ocean between 500 m and 1500 m. This dipole structure is the most robust feature throughout the entire evolution of salinity anomalies in the North Atlantic.

The evolution of salinity anomalies at the multicentennial timescale is closely linked to the AMOC's evolution. The downward and southward movements of salinity anomalies north of 45°N correspond to a strong convection or vertical mixing, and the mean advection by the lower branch of the AMOC, respectively. The northward and upward movements of anomalies south of 45°N go roughly within 26.5-27.6 σ_θ, corresponding to the mean advection through the upper branch of the AMOC. These two anomalies circulate in the North Atlantic, changing their phases during their movements (Fig. 4). In the South Atlantic, salinity anomalies do not reflect evolution synchronous with the AMOC.

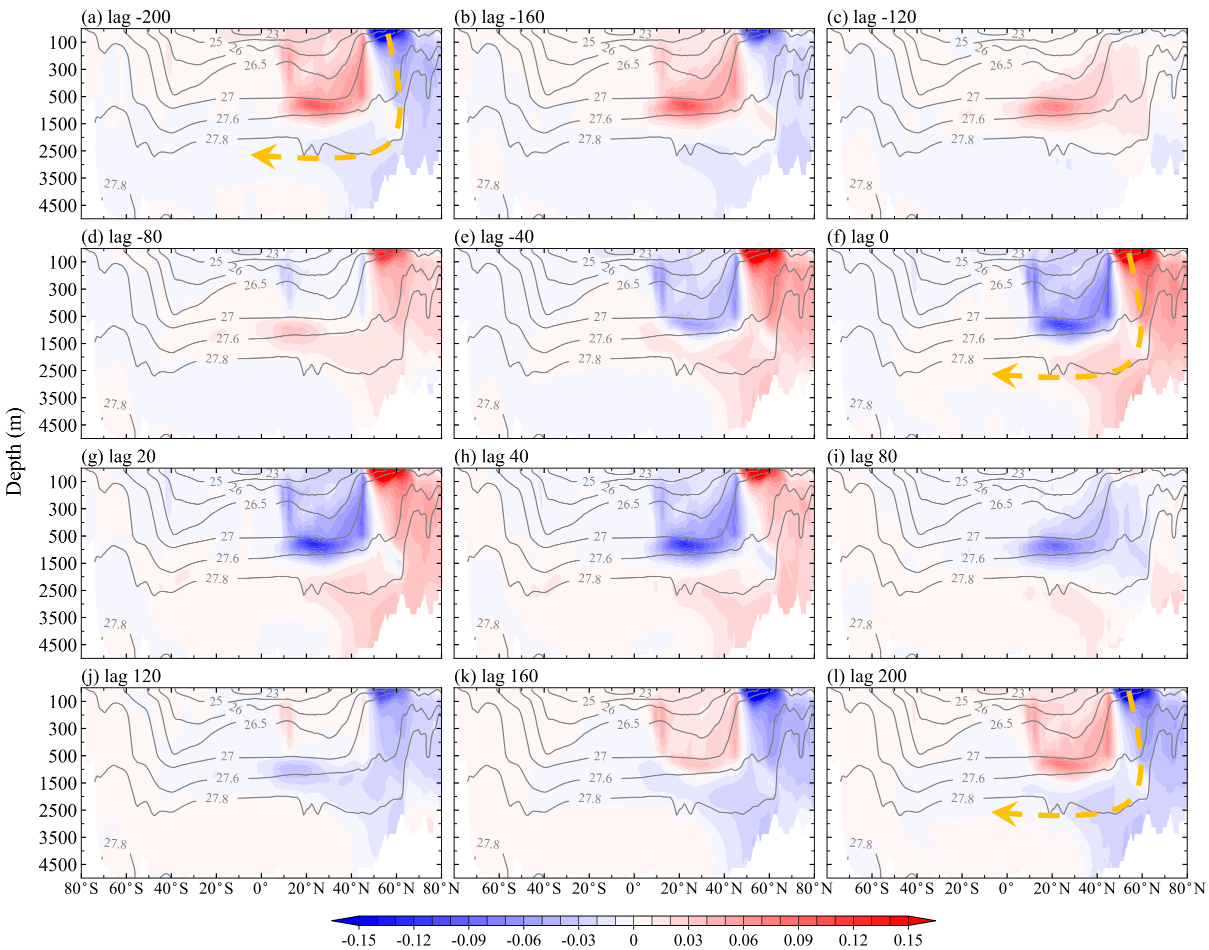

FIG. 4. Lead/lag regression coefficients of zonally averaged salinity anomalies in the Atlantic on the AMOC LFC1 (shading; units: psu). Negative lag means the AMOC LFC1 lags the salinity anomalies (units: year). Contours show the zonally averaged climatological potential density σ_θ in the Atlantic (units: kg m^{-3}). Orange arrows in (a), (f), and (l) show schematically the downward and southward movements of salinity anomalies.

Specifically, during the period when the salinity anomalies lead the AMOC by 200-120 years (Figs. 4a-c), salinity anomalies north of 45°N are negative and the AMOC is in its weak regime. The magnitude of negative anomalies decreases with time, indicating an ongoing phase transition from the weak to the strong AMOC regime. The positive anomaly in the subtropical intermediate ocean moves northward from about 40°N and upward along 26.5-27.6 σ_θ (Fig. 4c), neutralizing the negative anomaly in the DWF region and furthering its phase shift to positive (Fig. 4d). When the salinity anomalies lead the AMOC by 80-0 years, positive anomalies north of 45°N develop gradually (Figs. 4d-f) and eventually reach the maximum magnitude at lag 0 years (Fig. 4f), exhibiting a similar evolution to that of the AMOC. Anomaly in the upper DWF region is transported downward through convection or vertical mixing, then propagates southward in the deep ocean (Fig. 4, orange arrows). Meanwhile, negative anomalies grow in lower latitudes at 26.5-27.6 σ_θ. Afterward, the AMOC starts to decrease and the evolution of salinity anomalies enters the opposite phase (Figs. 4g-l). Throughout the entire cycle, salinity anomalies in the Arctic Ocean and Atlantic deep ocean are largely synchronized with that in the upper DWF region. Signals in the South Atlantic are much weaker compared to those in the North Atlantic.

Overall, the major evolution characteristics of salinity anomalies in the North Atlantic are reflected in three levels: (i) the upper ocean around 0-200 m, where the DWF region salinity anomaly is the strongest and develops locally, (ii) the intermediate ocean around 26.5-27.6 σ_θ, where the salinity anomalies south of 45°N evolve, and propagate northward to weaken the salinity anomaly in the upper DWF region, and (iii) the deep ocean around 27.8 σ_θ, where the salinity anomalies originate from the upper DWF region and propagate southward.

Figure 5 clearly shows the local development of salinity anomaly in the upper DWF region and the northward (southward) propagation of salinity anomaly in the intermediate (deep) ocean. Based on Fig. 4, we vertically average the anomalies over these three levels and then calculate their lead/lag regression coefficients on the AMOC LFC1. In the upper ocean (Fig. 5a), the most remarkable signal is in 45°-65°N, showing a local periodic evolution without a robust connection with signals in both the subtropical and polar regions. In the 26.5-27.6 σ_θ intermediate ocean (Fig. 5b), anomaly at 45°N propagates northward (white arrows), suggesting its potential influence on the DWF region. Anomaly near 20°N appears to develop locally with the opposite sign to that north of 45°N. In the 27.75-27.85 σ_θ deep ocean (Fig. 5c), anomalies propagate southward from the subpolar to equatorial and South Atlantic (white arrows). In all these three levels, the maximum regression coefficient in the subpolar region occurs when the salinity anomalies lead the AMOC LFC1 by around 10 years (Fig. 5, orange dot).

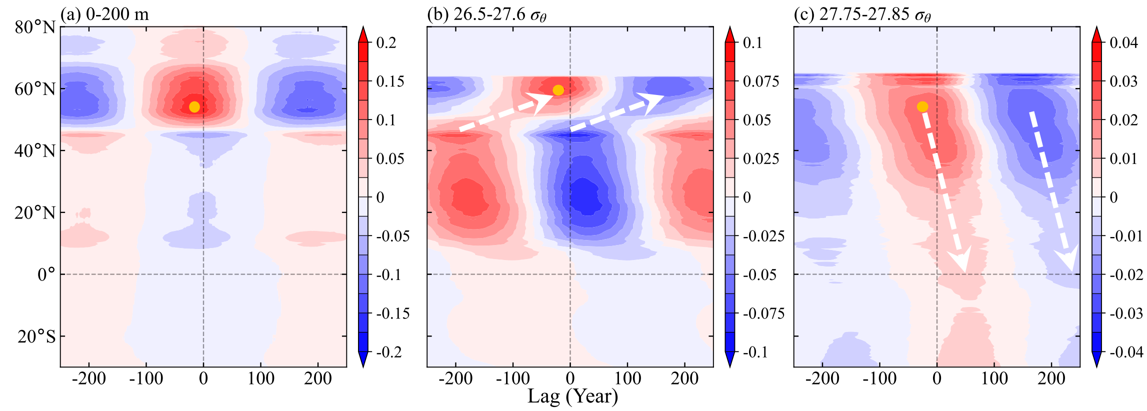

FIG. 5. Lead/lag regression coefficients of zonally and vertically averaged salinity anomalies in the Atlantic on the AMOC LFC1 (units: psu). (a) Averaged over 0-200 m, (b) averaged over 26.5-27.6 σ_θ, and (c) averaged over 27.75-27.85 σ_θ. The orange dot denotes the position of the maximum regression coefficient. In (b) and (c), salinity anomalies shallower than 200 m or north of 65°N are removed. The dashed white arrows show schematically the meridional propagations of salinity anomalies in the intermediate-deep oceans. Note that the colorbars for the three subplots are different. Negative lag means the AMOC LFC1 lags the salinity anomalies (units: year).

b. Horizontal patterns

To depict and also to explain the evolutions of salinity anomalies in these three levels, their horizontal lead/lag regression maps on the AMOC LFC1 are plotted in Figs. 6, 8, and 10, superimposed with climatological currents. In the North Atlantic upper ocean, the climatological currents feature the northward Gulf Stream and its eastward extension, the northeastward NAC, and the subpolar cyclonic circulation occupying the Labrador Sea and Irminger Sea (Fig. 6). Due to the blocking of the "transition zone", meridional mean currents at boundary 1 are only obvious in the east. Mean currents at boundaries 2, 3 are significantly weaker than those at boundary 1. Therefore, evident effect of mean advection of salinity anomaly on the DWF region is only possible at boundary 1. Even so, salinity anomaly in the DWF region evolves mostly locally without clear influence from mean advection. For example, when salinity anomaly in the DWF region evolves from negative to positive (Figs. 6a-f), it is always in antiphase with the subtropical salinity anomaly, and no continuous propagation of salinity anomaly through mean advection is clearly reflected. Similarly, when the DWF region salinity anomaly transitions from positive to negative (Figs. 6g-l), there is also little contribution from mean advection of subtropical salinity anomaly. When salinity anomaly in the upper DWF region is neutral (Figs. 6c, i), there appears to be weak salinity anomaly in the subtropical upper ocean that is advected northeastward by the NAC across boundary 1, and then northwestward by the Irminger current. However, this mean advection of salinity anomaly is too weak and may not be enough to determine the weakening (Figs. 6a-c, g-i) and phase transition (Figs. 6c, i) of salinity anomaly in the DWF region.

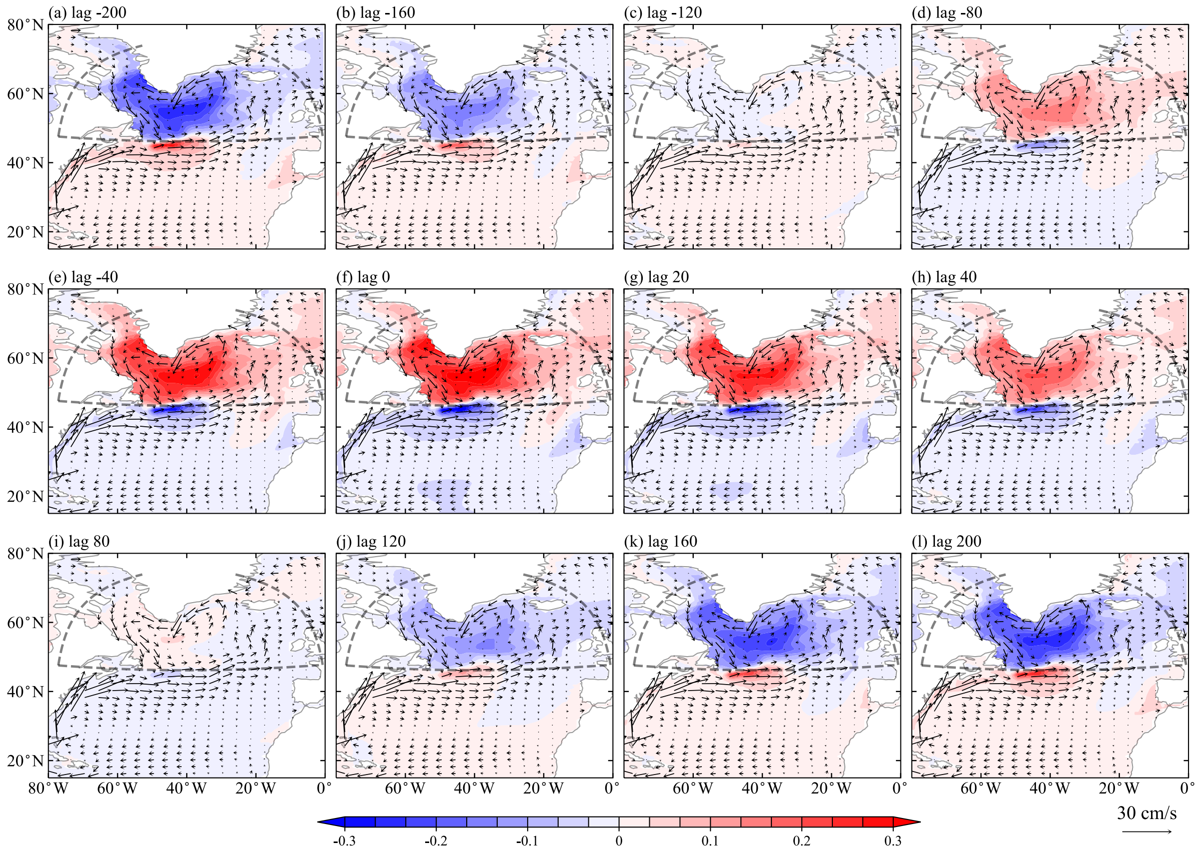

FIG. 6. Lead/lag regression coefficients of salinity anomalies averaged over 0-200 m on the AMOC LFC1 (units: psu), superimposed with climatological currents averaged over the same depth range (vector; units: cm s^{-1}). Negative lag means the AMOC LFC1 lags the salinity anomalies (units: year). Boundaries 1-3 defined in Fig. 2 are also plotted.

The growth of salinity anomaly in the upper DWF region (Figs. 6d-f, j-l) is controlled by the anomalous advection of mean salinity in the upper ocean. Figure 7 shows the lead/lag regression coefficients of current anomalies vertically averaged over 0-200 m on the AMOC LFC1, overlaid with climatological salinity. Current anomalies at boundaries 2, 3 are negligible throughout the entire cycle, indicating that the higher-latitude upper ocean has little effect on the DWF region salinity anomaly through anomalous advection of mean salinity. During the enhancing period of the positive DWF region salinity anomaly (Figs. 6d-f), the eastward and northward NAC is also intensifying (Figs. 7d-f), transporting more saline water from the mid-latitude eastern Atlantic to the DWF region and enhancing the positive salinity anomaly therein. Similarly, during the enhancing period of the negative DWF region salinity anomaly (Figs. 6j-l), the eastward and northward NAC is weakening

(Figs. 7j-l), reducing the northward transport of saline water from the mid-latitude eastern Atlantic and hence enhancing the negative DWF region salinity anomaly. Therefore, salinity anomaly in the upper DWF region and thus the AMOC anomaly are always enhanced by the anomalous advection in the subtropical-subpolar upper ocean. This is the well-known positive salinity advection feedback between AMOC anomaly and anomalous advection of mean salinity (Stommel 1961; Nakamura et al. 1994; Marotzke and Stone 1995; Sévellec et al. 2006).

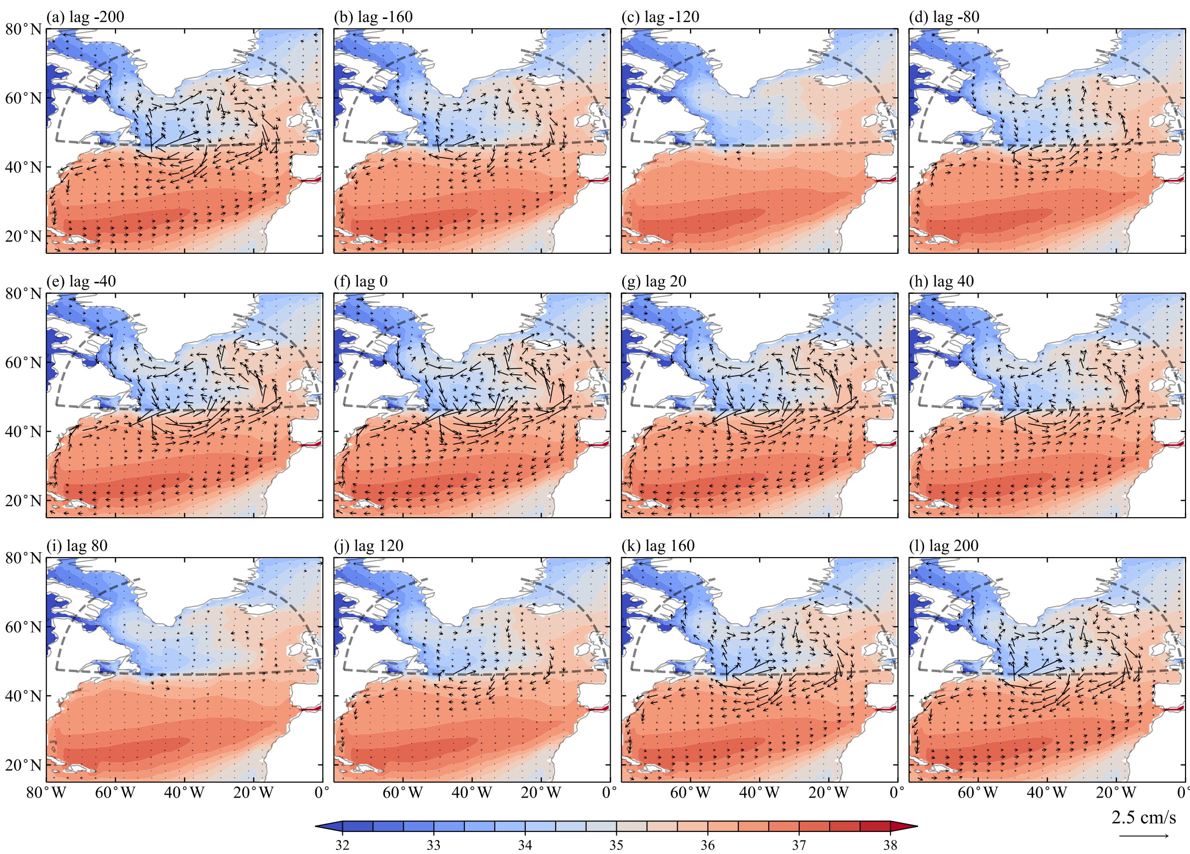

FIG. 7. Lead/lag regression coefficients of current anomalies averaged over 0-200 m on the AMOC LFC1 (units: cm s^{-1}), superimposed with climatological salinity averaged over the same depth range (shading; units: psu). Negative lag means the AMOC LFC1 lags the current anomalies (units: year).

It is the mean advection of salinity anomaly in the intermediate ocean that weakens the salinity anomaly in the upper DWF region. In the intermediate North Atlantic (Fig. 8), clear mean advection of salinity anomaly from the mid-latitude eastern Atlantic into the DWF region is reflected, having larger influence on the DWF region than that in the upper ocean. Salinity anomalies shallower than 200 m are removed, resulting in white areas in most of the subpolar basin (Fig. 8), where the climatological density exceeds 27.6 σ_θ. When salinity anomaly in the upper DWF region changes from negative to positive (Figs. 6a-f), the mid-latitude salinity anomaly with the opposite sign is advected eastward, northward, and upward by the mean NAC along isopycnals (Figs. 8a-f), weakening salinity anomaly in the upper DWF region and contributing to its phase change. Similar scenario also occurs when salinity anomaly in the upper DWF region changes from positive to negative (Figs. 6g-l, 8g-l). This is the negative feedback between AMOC anomaly and mean advection of salinity anomaly. When weakening processes outweigh enhancing processes for salinity anomaly in the upper DWF region, its magnitude peaks and starts to decrease (Figs. 6a, f, l), facilitating its cyclic evolution.

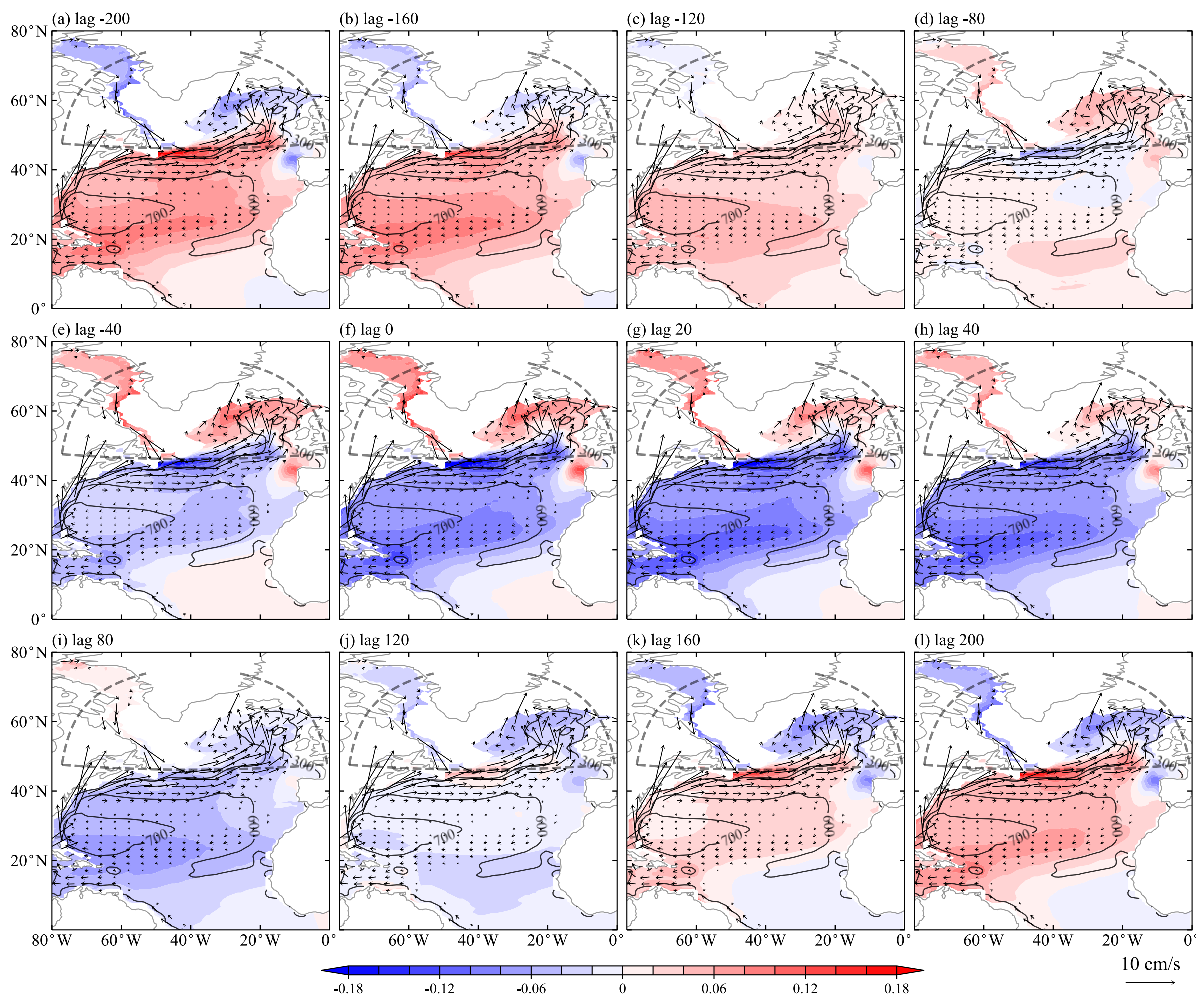

FIG. 8. Same as Fig. 6, but for variables averaged over 26.5-27.6 σ_{θ}. Black contours represent mean depths of 26.5-27.6 σ_{θ} (units: m). Currents weaker than 0.4 cm s^{-1} are not plotted. The 0-200 m salinity and current anomalies are removed to exclude the influence from the upper ocean, resulting in the blank regions in the subpolar basin.

Both Figs. 8 and 5b depict a distinct salinity anomaly in the 10°-35°N subtropical intermediate ocean, which is consistently out of phase with that in the upper DWF region. Analysis reveals that, this subtropical intermediate salinity anomaly is enhanced primarily by the anomalous equatorial western boundary current (WBC), and weakened by the northward mean advection along the Gulf Stream; surface processes as well as the vertical transport between the deep and intermediate oceans exert only marginal effects (figure not shown). From lag -200 to -120 years (Figs. 8a-c), the mean Gulf Stream moves positive salinity anomaly away from the subtropics into higher latitudes, contributing to the weakening of the subtropical positive salinity anomaly. On the other hand, the southeastward equatorial WBC anomaly reduces freshwater transport from the equatorial region into the subtropics (Figs. 9a-c), hence enhancing the subtropical positive salinity anomaly. When the subtropical salinity anomaly grows from slightly negative to the maximum negative value (Figs. 8e-g), the mean Gulf Stream removes negative salinity anomaly northward, thereby again counteracting the growth of the subtropical salinity anomaly. As the equatorial WBC anomaly turns northwestward (Figs. 9e-g), it transports more freshwater into the subtropics and enhances the negative salinity anomaly therein.

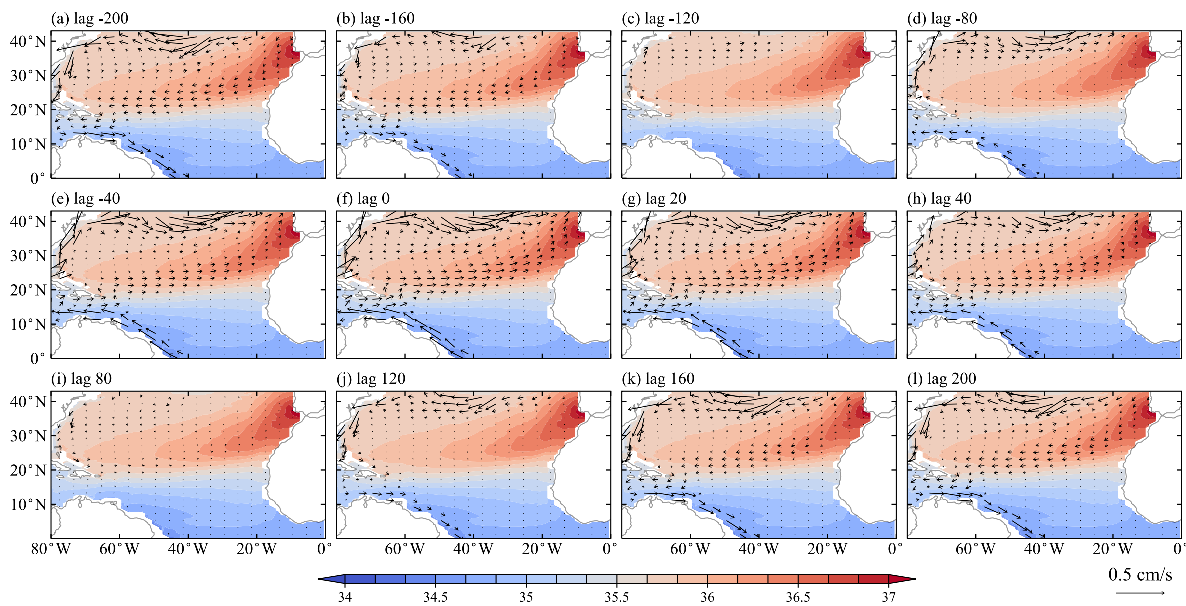

FIG. 9. Same as Fig. 7, but for variables averaged over 26.5-27.6 σ_θ. The 0-200 m salinity and current anomalies are removed to exclude the influence from the upper ocean.

In the deep ocean (Fig. 10), the evolution of salinity anomalies is dominated by the mean advection. Salinity anomalies are coherently advected southward from the subpolar basin to the tropics and South Atlantic, through the mean southward currents especially the Deep Western Boundary Current (DWBC). Salinity anomalies in the deep ocean exhibit nearly uniform polarity in the whole basin, consistent with the polarity of that in the upper DWF region. The newly developed positive and negative salinity anomalies in the subpolar North Atlantic (Figs. 10c, i) reach the South Atlantic in approximately 50 years (Figs. 10d, j). Their magnitude decreases along the route, as also observed in Fig. 5c.

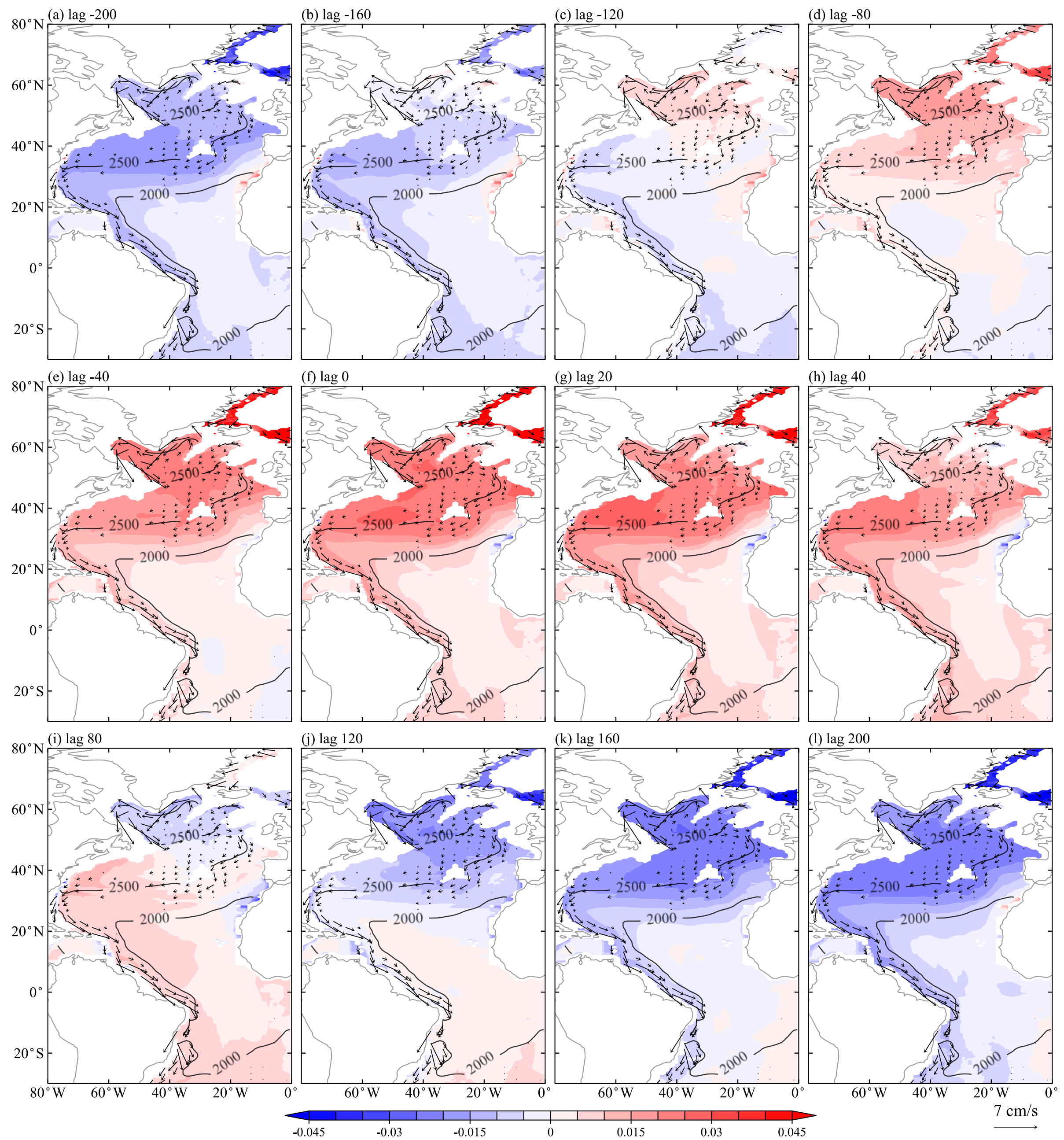

FIG. 10. Same as Fig. 8, but for variables averaged over 27.75-27.85 σ_θ. Black contours represent mean depths of 27.75-27.85 σ_θ (units: m). Currents weaker than 0.07 cm s^{-1} are not plotted. The 0-200 m salinity and current anomalies are removed to exclude the influence from the upper ocean, resulting in the blank regions in the subpolar basin.

c. Summary on collaborative salinity and AMOC evolutions

Now, a three-dimensional picture of the salinity evolution in conjunction with the AMOC appears. Starting from the freshest upper DWF region and thus the weakest AMOC (Fig. 6a), the mean NAC transports positive salinity anomaly northeastward and upward from the mid-latitude intermediate ocean to the upper DWF region (Figs. 8a-c), weakening the negative salinity anomaly therein (Figs. 6a-c). Meanwhile, the southward NAC anomaly on the eastern flank of boundary 1 reduces the transport of saline subtropical upper water into the DWF region, counteracting the intermediate ocean mean advection. Salinity anomaly in the subtropical intermediate ocean is positive and in antiphase with that in the upper DWF region. It is weakened by the mean Gulf Stream through losing positive salinity anomaly northward, enhanced mainly by the southeastward equatorial WBC anomaly which leads to less northward equatorial freshwater transport, and hardly affected by the deep ocean. Concurrently, negative salinity anomaly in the upper DWF region quickly descends to the deep ocean (Figs. 4a-c) and moves southward through the mean DWBC (Figs. 10a-c). These processes take about 80-90 years in total, followed by phase changes of salinity anomalies in the upper DWF region and subtropical intermediate ocean (Figs. 6d, 8e). Afterward, the newly developed positive AMOC anomaly and salinity anomaly in the upper DWF region strengthen themselves through the positive salinity advection feedback, realized as the anomalous NAC's northward advection of mean salinity (Figs. 7d-f). The strengthened positive AMOC anomaly also enhances the negative salinity anomaly in the intermediate subtropics (Figs. 8e-g), through increasing the northward freshwater transport from the equatorial region (Figs. 9e-g). The positive salinity anomaly in the upper DWF region is transported downward (Figs. 4d-f) and then carried southward (Figs. 10d-f) through the mean DWBC. These processes also take about 80-90 years. Now, a half cycle of the evolutions of salinity anomalies and the AMOC is completed, taking about 180 years in total. Subsequently, the weakening processes for salinity anomaly in the upper DWF region surpass the enhancing processes, and the evolutions of salinity and AMOC anomalies enter the opposite phase.

5. Determinant processes of the AMOC MCO

a. North Atlantic advection controls salinity anomaly in the upper DWF region

Salinity anomaly in the upper DWF region primarily originates from the anomalous advection of mean salinity and mean advection of salinity anomaly in the subtropical-subpolar North Atlantic. For the 0-1000 m DWF region, the freshwater mass budget comprises four components: (1) total

(Eulerian-mean + eddy-induced velocities) liquid freshwater mass transport at boundary 1; (2) total liquid freshwater mass transport at boundaries 2, 3; (3) surface freshwater mass flux induced by evaporation, precipitation, river runoff, and sea ice-related processes; and (4) total liquid freshwater mass transport at the 1000 m bottom. Lead/lag regression analysis of these freshwater budget components on the AMOC LFC1 is conducted in Fig. 11. S_{ref} in Eqs. (1) and (2) is given as 35.1 psu, the spatially averaged climatological salinity of the 0-1000 m DWF region.

Of the four aforementioned processes affecting salinity anomaly of the 0-1000 m DWF region, the most significant is the liquid freshwater transport at boundary 1 (Fig. 11a, black curve); vertical transport at the bottom is the least impactful (Fig. 11a, red curve). Freshwater transport at boundary 1 diminishes freshwater input of the DWF region when the AMOC is stronger than usual, enhancing the anomalies of the DWF region salinity and AMOC. In contrast, freshwater transport at boundaries 2, 3 (Fig. 11a, orange curve) weakens the AMOC anomaly, and is about half the magnitude of that of boundary 1. However, decomposition of the total liquid freshwater transport into components induced by the anomalous and mean advections in Fig. 11b reveals that, the anomalous and mean advections at boundary 1 (Fig. 11b, black curves) are about 20 and 4 times stronger than at boundaries 2, 3 (Fig. 11b, orange curves), respectively. Specifically, anomalous advection of mean salinity at boundary 1 (Fig. 11b, solid black curve) enhances salinity anomaly in the DWF region, manifesting the positive salinity advection feedback. Mean advection of salinity anomaly weakens salinity anomaly in the DWF region (Fig. 11b, dashed black curve), offsetting the anomalous advection of mean salinity to a large extent. As the regression coefficient of the anomalous advection-induced freshwater transport at boundaries 2, 3 shares the same sign as that of the mean advection-induced transport (Fig. 11b, orange curves), but those of boundary 1 are in antiphase with each other, Fig. 11a gives the impression that the effect of boundary 1 (Fig. 11a, black curve) on the DWF region salinity anomaly is only two times that of boundaries 2, 3 (Fig. 11a, orange curve). In fact, the actual determinants of the DWF region salinity anomaly are the anomalous and mean advections at 0-1000 m boundary 1.

The surface freshwater flux into the DWF region (Fig. 11c, solid black curve) is predominantly attributed to sea ice-related processes (Fig. 11c, dashed black curve). Sea ice-induced freshwater flux into the DWF region decreases when the AMOC is stronger than usual, further enhancing the AMOC anomaly. Surface freshwater flux into the Arctic Ocean region enclosed by boundaries 2, 3, and the Bering Strait, but excluding the Hudson Bay and Baltic Sea, is also evaluated (Fig. 11c, solid orange curve). During a stronger AMOC, more sea ice is melted in the Arctic Ocean (Fig. 11c, dashed orange curve). On the one hand, this increases the mean advection of salinity anomaly into the DWF region at boundaries 2, 3 (Fig. 11b, dashed orange curve). On the other hand, this reduces the sea ice transport into the DWF region and the further sea ice melting-induced freshwater flux therein (Fig. 11c, dashed black curve). Consequently, the effects of boundaries 2, 3 on the positive (negative) salinity anomaly in the DWF region during a stronger (weaker) AMOC are dual: weaken it through the increased (reduced) mean advection-induced liquid freshwater import, and enhance it through the reduced (increased) sea ice import. These two processes counteract each other, rendering the cumulative contribution of boundaries 2, 3 to the DWF region salinity anomaly less pronounced than when considered in isolation. This further underscores that the most decisive processes for salinity anomaly in the 0-1000 m DWF region, and thus this North Atlantic Ocean-originated AMOC MCO, are the anomalous advection of mean salinity and mean advection of salinity anomaly in the subtropical-subpolar North Atlantic.

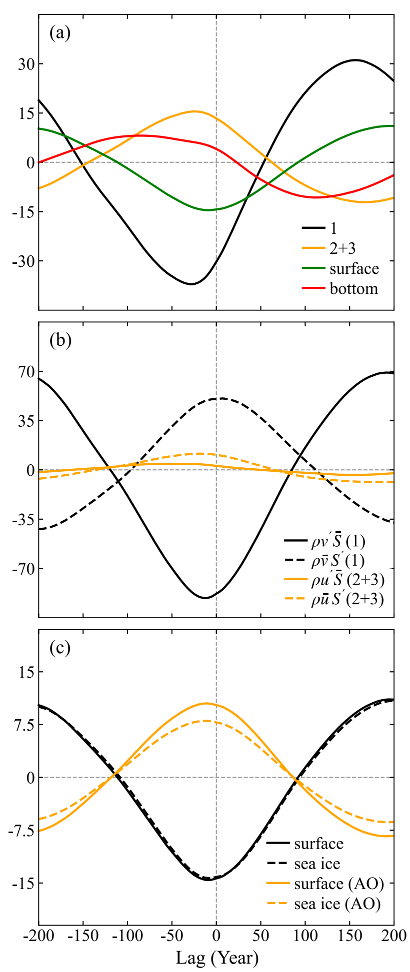

FIG. 11. Lead/lag regression coefficients of freshwater mass budget components induced by different processes onto the AMOC LFC1 (units: 10^6 kg s^{-1}). (a) Total liquid freshwater mass transports into the 0-1000 m DWF region

at boundary 1 (black curve), boundaries 2 and 3 (orange curve). Surface freshwater mass flux into the DWF region (green curve). Total liquid freshwater mass transport at the 1000 m bottom of the DWF region (red curve). (b) Liquid freshwater mass transports into the 0-1000 m DWF region at boundary 1, induced by the anomalous advection of mean salinity (solid black curve) and mean advection of salinity anomaly (dashed black curve). The orange curves are the same as the black curves, but for boundaries 2, 3. (c) Surface freshwater mass flux into the DWF region (solid black curve) and its sea ice-induced component (dashed black curve). The orange curves are the same as the black curves, but for the Arctic Ocean region encircled by boundaries 2, 3, and the Bering Strait (not annotated in figures), but excluding the Hudson Bay and Baltic Sea. Negative lag means the AMOC LFC1 lags the freshwater terms (units: year).

b. Indispensability of the North Atlantic anomalous and mean advections

Utilizing the North Atlantic-only box model in LY22 (appendix), we will examine whether this North Atlantic Ocean-originated AMOC MCO can occur when either the anomalous advection or the mean advection in the AMOC's upper limb is artificially deactivated. The theoretical model does not distinguish between the upper and intermediate oceans. In the upper branch, the anomalous advection of mean salinity and mean advection of salinity anomaly are represented by $q'\left(\overline{S_1}-\overline{S_2}\right)$ and $\overline{q}(S_1'-S_2')$, respectively. Starting with a positive q', $q'\left(\overline{S_1}-\overline{S_2}\right)$ increases S_2' and further strengthens q', constituting the positive salinity advection feedback. Concurrently, $q'\left(\overline{S_4}-\overline{S_1}\right)$ renders S_1' negative through increasing freshwater transport from subtropical deeper box 4 into subtropical upper box 1. The negative S_1' is then advected northward through $\overline{q}(S_1'-S_2')$, weakening the positive S_2' and thus the positive q'. This constitutes the mean advection process. $q'\left(\overline{S_4}-\overline{S_1}\right)$ represents a difference between the CESM1 simulation and the theoretical model. In the CESM1 simulation, the major anomalous advection that affects salinity anomaly in the subtropics is horizontal and originated from the equatorial region (Fig. 9). However, the paramount processes contributing to the DWF region salinity anomaly: anomalous and mean advections in the subtropical-subpolar North Atlantic, are present in both the CESM1 simulation and theoretical model.

When Eq. (A) is active, a self-sustained AMOC oscillation is exhibited in the theoretical model (Fig. 12a). When artificially deactivating the anomalous advection in the upper branch [$q'\left(\overline{S_1}-\overline{S_2}\right)$] while leaving other processes unmodified, the AMOC exhibits a strongly damped oscillation (Fig. 12b), because of the absence of the positive salinity advection feedback that enhances the AMOC anomaly. On the other hand, when the mean advection in the upper branch [$\overline{q}(S_1'-S_2')$] is deactivated, its weakening effect on the AMOC anomaly is eliminated, therefore leading to a runaway tendency for q' (Fig. 12c). This further reveals the indispensability of the anomalous and mean advections in the upper AMOC limb for the North Atlantic Ocean-originated AMOC MCO.

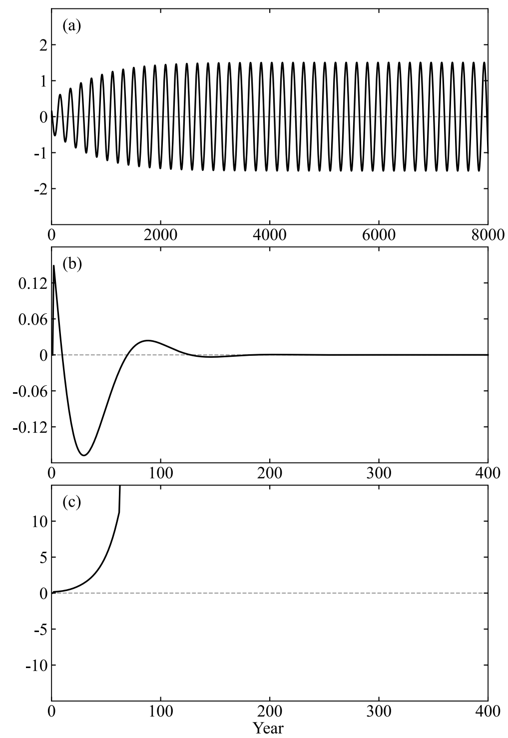

FIG. 12. (a) Self-sustained oscillation of the AMOC anomaly q' (units: Sv) in the theoretical model (appendix). (b) Damped oscillation of q' when the anomalous advection of mean salinity $q'\left(\overline{S_1}-\overline{S_2}\right)$ in the upper branch is deactivated. (c) Runaway q' when the mean advection of salinity anomaly $\overline{q}(S_1'-S_2')$ in the upper branch is deactivated.

6. Summary and discussion

An MCV of the AMOC is identified in a CESM1 control simulation. It is interpreted as a linear oscillation and can be termed an MCO. This AMOC MCO is primarily driven by processes in the North Atlantic, thereby potentially representing a North Atlantic Ocean-originated mode of the real-world AMOC MCV. In the upper level of the DWF region in the subpolar North Atlantic, variation of salinity anomaly dominates variation of density anomaly, leading to the AMOC oscillation. The most determinant processes for salinity anomaly in the upper DWF region, and thus the AMOC MCO, are the anomalous advection of mean salinity and mean advection of salinity anomaly in the subtropical-subpolar North Atlantic (Fig. 11b, black curves), which have much greater effects than other processes. Contribution from the bottom of the DWF region is negligible. The Arctic Ocean exerts two counteractive effects on this AMOC MCO. First, a positive AMOC anomaly increases Arctic Ocean sea ice melting, resulting in a negative salinity anomaly therein that can be advected into the DWF region through mean advection. This curbs the AMOC anomaly. Second, as more sea ice melts in the Arctic Ocean, there is a reduction in sea ice transport into the DWF region, thus decreasing the melting-induced freshwater input of the DWF region. This enhances the AMOC anomaly. Overall, the cumulative effect of the Arctic Ocean on this AMOC MCO is relatively minor, and much weaker than the anomalous and mean advections in the North Atlantic. Additionally, no obvious salinity anomaly that evolves synchronously with the AMOC is observed in the South Atlantic or Southern Ocean. Therefore, it is appropriate to designate this AMOC MCO as a North Atlantic Ocean-originated AMOC MCO.

Figure 13 schematically summarizes the core processes for this AMOC MCO, with an emphasis on advection in the North Atlantic. At the AMOC's negative peak (Fig. 13a), both the NAC and equatorial WBC display southward anomalies (Fig. 13a, dashed blue arrows). The negative salinity anomaly in the upper DWF region is enhanced by the southward NAC anomaly (Fig. 13a, upper dashed blue arrow) through the reduced northward subtropical saline water transport, and weakened by the northward mean advection (Fig. 13, upper solid black arrow) that carries the positive salinity anomaly in the subtropical intermediate ocean northward. Salinity anomaly in the upper DWF region constantly descends through the subpolar convection or vertical mixing, then moves southward through the mean DWBC (Fig. 13, lower solid black arrow). The positive salinity anomaly in the subtropical intermediate ocean is weakened by the northward mean advection that carries salinity anomaly away northward, and enhanced by the reduced northward freshwater transport induced by the southward equatorial WBC anomaly (Fig. 13a, lower dashed blue arrow). At this stage, weakening processes for the negative (positive) salinity anomaly in the upper DWF region (subtropical intermediate ocean) are stronger than enhancing processes, hence the negative DWF region (positive subtropical intermediate) salinity anomaly is weakening.

After the phase transition (Fig. 13b), anomalies of the upper DWF region salinity and AMOC turn slightly positive, as do the NAC and equatorial WBC (Fig. 13b, dashed orange arrows). These anomalies are subsequently strengthened by the positive salinity advection feedback. The subtropical intermediate salinity anomaly lags slightly behind that in the upper DWF region, and is still undergoing its phase transition. Later, it turns negative and is strengthened by the increased northward freshwater transport through the northward equatorial WBC anomaly. When enhancing processes for salinity anomaly in the upper DWF region are surpassed by weakening processes, the positive AMOC anomaly peaks (Fig. 13c) and starts to neutralize. Subsequently, the AMOC anomaly turns negative (Fig. 13d) and progresses toward the negative peak (Fig. 13a), completing a full cycle.

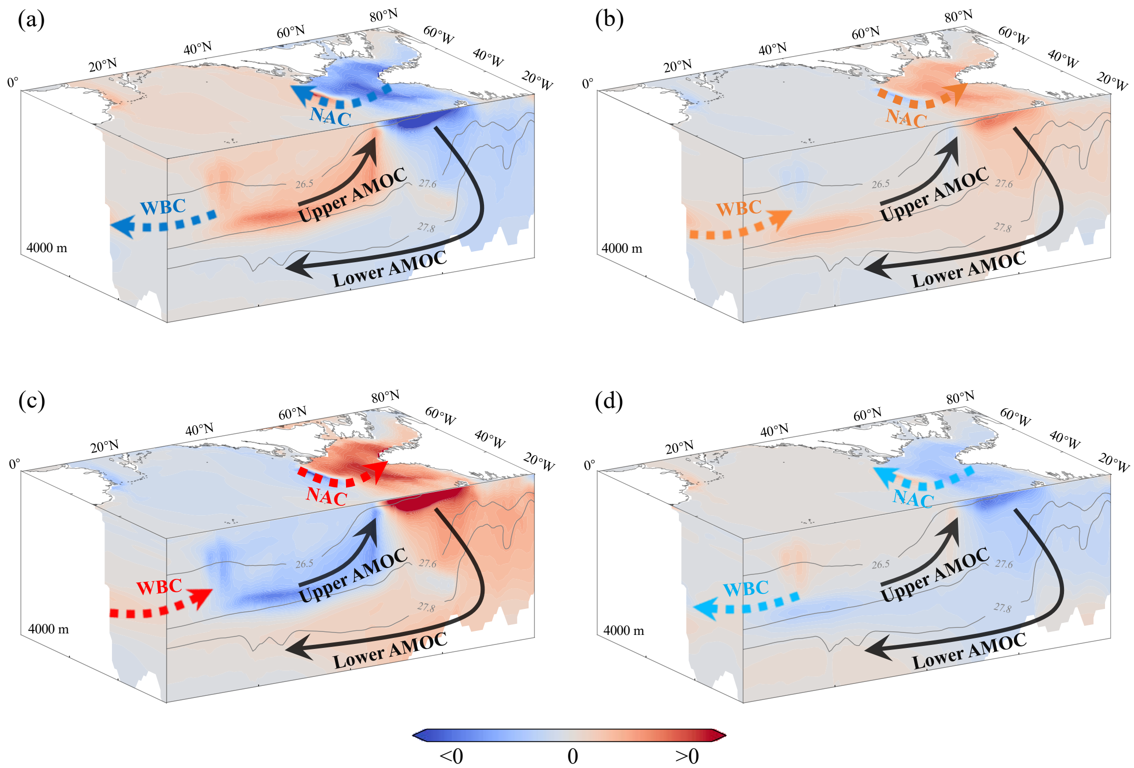

FIG. 13. Schematic diagrams showing oceanic states in the North Atlantic during (a) the peak of the negative phase, (b) the start of the positive phase, (c) the peak of the positive phase, and (d) the start of the negative phase of the AMOC multicentennial oscillation (MCO). Dashed and solid arrows represent anomalous and mean currents, respectively.

Significance of the two paramount processes for this AMOC MCO: the anomalous and mean advections in the upper AMOC branch, is tested utilizing the theoretical model in LY22. When both processes are active, the theoretical model exhibits a pronounced AMOC MCO. Equations of the theoretical model [Eq. (A)], which capture the essence of this modeled North Atlantic Ocean-originated AMOC MCO, can mathematically explain the enhancing and weakening effects of the anomalous and mean advections on the AMOC anomaly. If either the anomalous or mean advection in the upper branch is artificially deactivated, the theoretical model cannot exhibit the AMOC MCO, emphasizing the essential role of these two advection processes in this North Atlantic Ocean-originated AMOC MCO.

The AMOC MCO analyzed in this study is North Atlantic Ocean-originated, differentiating it from the “flip-flop” AMOC MCO in Park and Latif (2008), the Southern Ocean-originated AMOC

MCO in Delworth and Zeng (2012), as well as the Arctic Ocean-originated AMOC MCO in Jiang et al. (2021) and Meccia et al. (2023). The “flip-flop” AMOC MCO represents a multi-equilibrium phenomenon that is markedly distinct from our study. The main difference between the Southern Ocean-originated AMOC MCO and our North Atlantic Ocean-originated AMOC MCO lies in the location of the salinity anomaly that is advected northward toward the DWF region by mean advection. In their study, mean advection moves salinity anomaly in the upper Southern Ocean northward, whereas in ours, the northward salinity anomaly originates from the subtropical intermediate ocean. In Jiang et al. (2021) and Meccia et al. (2023), clear current and salinity anomalies are exhibited north of the subpolar North Atlantic, yet in our study the anomalies therein are rather weak, especially the current anomalies. Given the connection between salinity anomalies from the Arctic Ocean and the sea ice thermodynamics, distinctions between the Arctic Ocean-originated and North Atlantic Ocean-originated AMOC MCOs likely stem from the difference in both the ocean model and the sea ice model utilized.

Despite these differences, our study still aids the understanding of other AMOC MCOs. The positive salinity advection feedback in the subtropical-subpolar upper ocean is pivotal not only in this study, but also in the Southern Ocean-originated and Arctic Ocean-originated AMOC MCOs. In Fig. 5a of Delworth and Zeng (2012), the continuous northward salinity anomaly that is symbolic of mean advection reaches approximately 45°N. North of 45°N, salinity anomalies evolve nearly synchronously, mirroring the corresponding pattern in Fig. 5a of our current study. Therefore, this local evolution of salinity anomaly is likely driven by the positive salinity advection feedback. Local salinity evolution north of 45°N is also reflected in Fig. 5a in Jiang et al. (2021) and Fig. 5a in Meccia et al. (2023), suggesting that the positive salinity advection feedback is also likely to be the enhancing process for AMOC anomaly in the Arctic Ocean-originated AMOC MCOs, which is not addressed in these two studies. The AMOC MCO identified in the intermediate-complexity model study of Mehling et al. (2023) has a similar mechanism to the Arctic Ocean-originated AMOC MCOs. They employed a box model adapted from Stommel (1961) to explain their AMOC MCO, and highlighted the Arctic Ocean-originated salinity anomaly by incorporating an additional Arctic Ocean box. Likewise, Wei and Zhang (2022) also utilized a revised Stommel’s two-box model incorporating a negative feedback representing salinity anomaly from the Arctic Ocean, to account for the Arctic Ocean-originated AMOC multidecadal oscillation. Its essence aligns closely with that of the Arctic Ocean-originated AMOC MCOs. Both theoretical models employed in these two studies actually incorporate the positive salinity advection feedback and mean advection process in the subtropical-subpolar upper ocean, although their focus is salinity anomaly from the Arctic Ocean. Hence, the subtropical-subpolar positive salinity advection feedback likely serves as the essential enhancing process for AMOC anomaly in the North Atlantic Ocean-originated, Southern Ocean-originated, and Arctic Ocean-originated AMOC MCOs. The primary difference among them is perhaps the origin of the salinity anomaly that is advected into the DWF region through mean advection. With the incorporation of additional boxes representing the South Atlantic/Southern Ocean, the theoretical model in LY22 has the potential to account for the South Ocean-originated AMOC MCO, through capturing salinity anomalies in the Southern Ocean.

To the best of our knowledge, this study is perhaps the first to identify the North Atlantic Ocean-originated AMOC MCO in coupled models. Therefore, this mode will be more convincing if identified in other coupled models. However, the assessments of whether this North Atlantic Ocean-originated AMOC MCO and other previously proposed AMOC MCOs genuinely exist in the Earth's climate system, as well as their relative contributions to the real-world AMOC MCV, are inhibited by the limited direct observations that are unfortunately unavailable in the foreseeable future. Given that the natural forcing remains constant in these coupled model simulations, these coupled model AMOC MCOs all represent internal variability. Therefore, the AMOC MCV might have been a background for the anthropogenic centennial climate change. Further research into the mechanisms of various potential modes that constitute the real-world AMOC MCV will enhance our understanding of the ongoing climate change.

Acknowledgements.

This research is jointly supported by the NSF of China (Nos. 42230403, 42288101, and 41725021) and by the foundation at the Shanghai Frontiers Science Centre of Atmosphere-Ocean Interaction of Fudan University. Prof. Q. Zhang acknowledges supports from Swedish Research Council (2022-03129).

Data Availability Statement.

All data used in this study are available upon request.

APPENDIX

In Li and Yang (2022), we proposed a North Atlantic-only theoretical model for AMOC multicentennial oscillation. The North Atlantic is divided into 4 boxes (Fig. A1): subtropical upper ocean box 1, subpolar upper ocean box 2, subpolar deeper ocean box 3, and subtropical deeper ocean box 4. Equilibrium (anomalous) salinities of boxes 1-4 are represented by $\overline{S_1}$ (S_1'), $\overline{S_2}$ (S_2'), $\overline{S_3}$ (S_3'), and $\overline{S_4}$ (S_4'), respectively. Climatological (anomalous) AMOC is represented by $\overline{q}$ (q'). Only salinity variation is considered here. The linearized salinity equations are:

$$V_1\dot{S}_1' = q'(\overline{S_4} - \overline{S_1}) + \overline{q}(S_4' - S_1') \quad \text{(A1)}$$

$$V_2\dot{S}_2' = q'\left(\overline{S_1} - \overline{S_2}\right) + \overline{q}(S_1' - S_2') - k_m(S_2' - S_3') \quad \text{(A2)}$$

$$V_3\dot{S}_3' = \overline{q}(S_2' - S_3') + k_m(S_2' - S_3') \quad \text{(A3)}$$

$$V_4\dot{S}_4' = \overline{q}(S_3' - S_4') \quad \text{(A4)}$$

$$q' = \lambda\Delta\rho' = \lambda\rho_0\beta[\delta(S_2' - S_1') + (1-\delta)(S_3' - S_4')] \quad \text{(A5)}$$

$$\delta = \frac{V_1}{V_1 + V_4} = \frac{V_2}{V_2 + V_3} = \frac{D_1}{D} \quad \text{(A6)}$$

where V_1, V_2, V_3, and V_4 are the volumes of boxes 1-4, respectively. λ is a linear closure coefficient, representing the sensitivity of AMOC anomaly to meridional density difference $\Delta\rho'$. ρ_0 and β are the reference sea water density and haline contraction coefficient. k_m is a nonlinear vertical mixing term parameterized as $\kappa q'^2$, with κ = 10^{-4} m^{-3} s.

In this study, the box model's geometry and parameters are set according to the CESM1 control simulation. Boxes 1-4 span the 10°-45°N and 0-1000 m, 45°-70°N and 0-1000 m, 45°-70°N and 1000-4000 m, and 10°-45°N and 1000-4000 m of the North Atlantic domain in the CESM1 model, respectively. Their volumes V_{1-4} are 2.65 $\times$ 10^{16} m^3, 0.77 $\times$ 10^{16} m^3, 1.16 $\times$ 10^{16} m^3, and 6.3 $\times$ 10^{16} m^3, respectively. $\overline{q}$ is set to 24 Sv, corresponding to the climatological AMOC (Fig. 1a). $\overline{S_{1-4}}$ are the climatological salinities of the CESM1 model domains corresponding to boxes 1-4. $\overline{S_1}$ is 35.9 psu. The actual values of $\overline{S_{2-4}}$ are all close to 35.2 psu, so they are collectively set to 35.2 psu for conciseness. ρ_0 and β are set to 10^3 kg m^{-3} and 7.61 $\times$ 10^{-4} psu^{-1}, respectively. Figure A2 suggests that in the CESM1 simulation, the AMOC anomaly is linearly proportional to the anomaly of difference in potential density between 45°-70°N and 10°-45°N North Atlantic. According to Fig. A2, λ is set to 70 Sv kg^{-1} m^{3}.

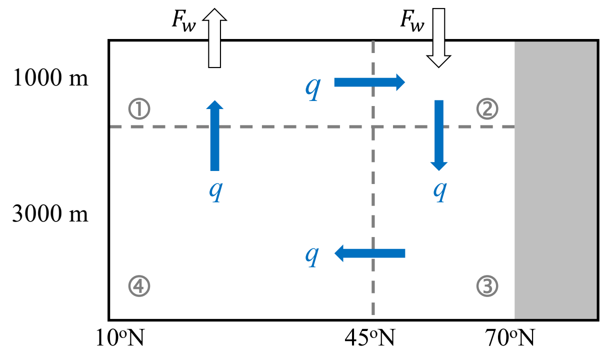

FIG. A1. Schematic of the 4-box ocean model. Ocean boxes are denoted by ①, ②, ③, and ④. Boxes 1 and 4 represent the upper and deeper subtropical oceans, respectively; boxes 2 and 3 represent the upper and deeper subpolar oceans, respectively. D_1 and D_2 are the depths of the upper and deeper boxes, respectively. F_w is the net freshwater flux out of (into) the subtropical (subpolar) surface ocean, which is cancelled out during the linearization to derive Eq. (A). q represents the AMOC strength.

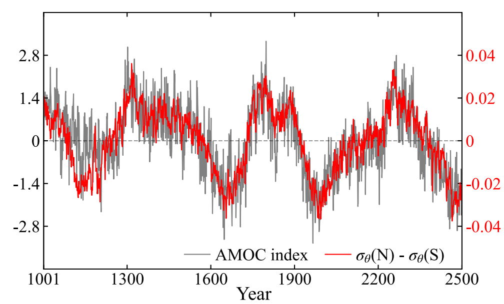

FIG. A2. Time series for the anomalies of AMOC index (gray curve, left y-axis; units: Sv) and difference in potential density σ_θ between the 45°-70°N and 10°-45°N North Atlantic (red curve, right y-axis; units: kg m^{-3}), in the CESM1 control simulation.

REFERENCES

Askjær, T. G., and Coauthors, 2022: Multi-centennial Holocene climate variability in proxy records and transient model simulations. *Quat. Sci. Rev.*, **296**, 20, https://doi.org/10.1016/j.quascirev.2022.107801

Ayache, M., D. Swingedouw, Y. Mary, F. Eynaud, and C. Colin, 2018: Multi-centennial variability of the AMOC over the Holocene: A new reconstruction based on multiple proxy-derived SST records. *Global Planet. Change*, **170**, 172-189, https://doi.org/10.1016/j.gloplacha.2018.08.016

Buckley, M. W., and J. Marshall, 2016: Observations, inferences, and mechanisms of the Atlantic Meridional Overturning Circulation: A review. *Rev. Geophys.*, **54**, 5-63, https://doi.org/10.1002/2015RG000493

Chabaud, L., M. F. S. Goni, S. Desprat, and L. Rossignol, 2014: Land-sea climatic variability in the eastern North Atlantic subtropical region over the last 14,200 years: Atmospheric and oceanic processes at different timescales. *Holocene*, **24**, 787-797, https://doi.org/10.1177/0959683614530439

Chapman, M. R., and N. J. Shackleton, 2000: Evidence of 550-year and 1000-year cyclicities in North Atlantic circulation patterns during the Holocene. *Holocene*, **10**, 287-291, https://doi.org/10.1191/095968300671253196

Craig, A. P., M. Vertenstein, and R. Jacob, 2012: A new flexible coupler for earth system modeling developed for CCSM4 and CESM1. *Int. J. High Perform. Comput. Appl.*, **26**, 31-42, https://doi.org/10.1177/1094342011428141

Delworth, T. L., and F. R. Zeng, 2012: Multicentennial variability of the Atlantic meridional overturning circulation and its climatic influence in a 4000 year simulation of the GFDL CM2.1 climate model. *Geophys. Res. Lett.*, **39**, https://doi.org/10.1029/2012GL052107

Drijfhout, S., C. Heinze, M. Latif, and E. MaierReimer, 1996: Mean circulation and internal variability in an ocean primitive equation model. *J. Phys. Oceanogr.*, **26**, 559-580, https://doi.org/10.1175/1520-0485(1996)026<0559:MCAIVI>2.0.CO;2

Fox-Kemper, B., and R. Ferrari, 2008: Parameterization of mixed layer eddies. Part II: Prognosis and impact. *J. Phys. Oceanogr.*, **38**, 1166-1179, https://doi.org/10.1175/2007JPO3788.1

Fox-Kemper, B., R. Ferrari, and R. Hallberg, 2008: Parameterization of mixed layer eddies. Part I: Theory and diagnosis. *J. Phys. Oceanogr.*, **38**, 1145-1165, https://doi.org/10.1175/2007JPO3792.1

Gent, P. R., and J. C. McWilliams, 1990: Isopycnal mixing in ocean circulation models. *J. Phys.*

Oceanogr., **20**, 150-155, https://doi.org/10.1175/1520-0485(1990)020<0150:IMIOCM>2.0.CO;2

Griffies, S. M., and E. Tziperman, 1995: A linear thermohaline oscillator driven by stochastic atmospheric forcing. *J. Climate*, **8**, 2440-2453, https://doi.org/10.1175/1520-0442(1995)008<2440:ALTODB>2.0.CO;2

Hall, I. R., G. G. Bianchi, and J. R. Evans, 2004: Centennial to millennial scale Holocene climate-deep water linkage in the North Atlantic. *Quat. Sci. Rev.*, **23**, 1529-1536, https://doi.org/10.1016/j.quascirev.2004.04.004

Hansen, B., S. Østerhus, H. Hátún, R. Kristiansen, and K. M. H. Larsen, 2003: The Iceland-Faroe inflow of Atlantic water to the Nordic Seas. *Prog. Oceanogr.*, **59**, 443-474, https://doi.org/10.1016/j.pocean.2003.10.003

Hughes, Tertia M. C., and Andrew J. Weaver, 1994: Multiple equilibria of an asymmetric two-basin ocean model. *J. Phys. Oceanogr.*, **24**, 619-637, https://doi.org/10.1175/1520-0485(1994)024<0619:MEOAAT>2.0.CO;2

Hunke, E. C., and W. H. Lipscomb, 2010: CICE: The Los Alamos Sea Ice Model, documentation and software user's manual, version 4.1. Los Alamos National Laboratory Rep. LACC-06-012, 76 pp.

Jiang, W. M., G. Gastineau, and F. Codron, 2021: Multicentennial variability driven by salinity exchanges between the Atlantic and the Arctic Ocean in a coupled climate model. *J. Adv. Model. Earth Syst.*, **13**, e2020MS002366, https://doi.org/10.1029/2020MS002366

Jin, F. F., 1997: An equatorial ocean recharge paradigm for ENSO. Part I: Conceptual model. *J. Atmos. Sci.*, **54**, 811-829, https://doi.org/10.1175/1520-0469(1997)054<0811:AEORPF>2.0.CO;2

Kieke, D., and I. Yashayaev, 2015: Studies of Labrador Sea Water formation and variability in the subpolar North Atlantic in the light of international partnership and collaboration. *Prog. Oceanogr.*, **132**, 220-232, https://doi.org/10.1016/j.pocean.2014.12.010

Kim, J. H., and Coauthors, 2004: North Pacific and North Atlantic sea-surface temperature variability during the Holocene. *Quat. Sci. Rev.*, **23**, 2141-2154, https://doi.org/10.1016/j.quascirev.2004.08.010

Kissel, C., A. Van Toer, C. Laj, E. Cortijo, and E. Michel, 2013: Variations in the strength of the North Atlantic bottom water during Holocene. *Earth Planet. Sci. Lett.*, **369**, 248-259, https://doi.org/10.1016/j.epsl.2013.03.042

Lawrence, D. M., and Coauthors, 2011: Parameterization improvements and functional and structural advances in version 4 of the Community Land Model. *J. Adv. Model. Earth Syst.*, **3**, 27, https://doi.org/10.1029/2011MS000045

Li, Y., and H. J. Yang, 2022: A theory for self-sustained multicentennial oscillation of the Atlantic meridional overturning circulation. *J. Climate*, **35**, 5883-5896, https://doi.org/10.1175/JCLI-D-21-0685.1

Liu, Z. Y., 2012: Dynamics of interdecadal climate variability: A historical perspective. *J. Climate*, **25**, 1963-1995, https://doi.org/10.1175/2011JCLI3980.1

Marotzke, J., 1996: Analysis of thermohaline feedbacks. *Decadal Climate Variability: Dynamics and Predictability*, D. L. T. Anderson, and J. Willebrand, Eds., Springer, 333-378.

Marotzke, J., and P. H. Stone, 1995: Atmospheric transports, the thermohaline circulation, and flux adjustments in a simple coupled model. *J. Phys. Oceanogr.*, **25**, 1350-1364, https://doi.org/10.1175/1520-0485(1995)025<1350:ATTTCA>2.0.CO;2

Martin, T., W. Park, and M. Latif, 2013: Multi-centennial variability controlled by Southern Ocean convection in the Kiel Climate Model. *Climate Dyn.*, **40**, 2005-2022, https://doi.org/10.1007/s00382-012-1586-7

——, 2015: Southern Ocean forcing of the North Atlantic at multi-centennial time scales in the Kiel Climate Model. *Deep-Sea Res. Part II-Top. Stud. Oceanogr.*, **114**, 39-48, https://doi.org/10.1016/j.dsr2.2014.01.018

McDermott, F., D. P. Mattey, and C. Hawkesworth, 2001: Centennial-scale Holocene climate variability revealed by a high-resolution speleothem delta 18O record from SW Ireland. *Science*, **294**, 1328-1331, https://doi.org/10.1126/science.1063678

Meccia, V. L., R. Fuentes-Franco, P. Davini, K. Bellomo, F. Fabiano, S. T. Yang, and J. von Hardenberg, 2023: Internal multi-centennial variability of the Atlantic meridional overturning circulation simulated by EC-Earth3. *Climate Dyn.*, 18, https://doi.org/10.1007/s00382-022-06534-4

Mehling, O., K. Bellomo, M. Angeloni, C. Pasquero, and J. von Hardenberg, 2023: High-latitude precipitation as a driver of multicentennial variability of the AMOC in a climate model of intermediate complexity. *Climate Dyn.*, 16, https://doi.org/10.1007/s00382-022-06640-3

Miettinen, A., D. Divine, N. Koc, F. Godtliebsen, and I. R. Hall, 2012: Multicentennial variability of the sea surface temperature gradient across the subpolar North Atlantic over the last 2.8 kyr. *J. Climate*, **25**, 4205-4219, https://doi.org/10.1175/JCLI-D-11-00581.1

Mikolajewicz, U., and E. Maier-Reimer, 1990: Internal secular variability in an ocean general circulation model. *Climate Dyn.*, **4**, 145-156, https://doi.org/10.1007/bf00209518

Mysak, L. A., T. F. Stocker, and F. Huang, 1993: Century-scale variability in a randomly forced, two-dimensional thermohaline ocean circulation model. *Climate Dyn.*, **8**, 103-116, https://doi.org/10.1007/bf00208091

Nakamura, M., P. H. Stone, and J. Marotzke, 1994: Destabilization of the thermohaline circulation by atmospheric eddy transports. *J. Climate*, **7**, 1870-1882, https://doi.org/10.1175/1520-0442(1994)007<1870:DOTTCB>2.0.CO;2

Neale, R. B., and Coauthors, 2010: Description of the Community Atmosphere Model (CAM 4.0). Technical Report NCAR/TN-485+STR, National Center for Atmospheric Research, Boulder, CO, 268

Newby, P. E., B. N. Shuman, J. P. Donnelly, K. B. Karnauskas, and J. Marsicek, 2014: Centennial-to-millennial hydrologic trends and variability along the North Atlantic coast, USA, during the Holocene. *Geophys. Res. Lett.*, **41**, 4300-4307, https://doi.org/10.1002/2014GL060183

Nyberg, J., B. A. Malmgren, A. Kuijpers, and A. Winter, 2002: A centennial-scale variability of tropical North Atlantic surface hydrography during the late Holocene. *Palaeogeogr. Palaeocl. Palaeoecol.*, **183**, 25-41, https://doi.org/10.1016/S0031-0182(01)00446-1

Oppo, D. W., J. F. McManus, and J. L. Cullen, 2003: Deepwater variability in the Holocene epoch. *Nature*, **422**, 277, https://doi.org/10.1038/422277b

Park, W., and M. Latif, 2008: Multidecadal and multicentennial variability of the meridional overturning circulation. *Geophys. Res. Lett.*, **35**, https://doi.org/10.1029/2008GL035779

Rivin, I., and E. Tziperman, 1997: Linear versus self-sustained interdecadal thermohaline variability in a coupled box model. *J. Phys. Oceanogr.*, **27**, 1216-1232, https://doi.org/10.1175/1520-0485(1997)027<1216:LVSSIT>2.0.CO;2

Roquet, F., G. Madec, T. J. McDougall, and P. M. Barker, 2015: Accurate polynomial expressions for the density and specific volume of seawater using the TEOS-10 standard. *Ocean Modell.*, **90**, 29-43, https://doi.org/10.1016/j.ocemod.2015.04.002

Sévellec, F., T. Huck, and M. Ben Jelloul, 2006: On the mechanism of centennial thermohaline oscillations. *J. Mar. Res.*, **64**, 355-392, https://doi.org/10.1357/002224006778189608

Smith, R. D., and Coauthors, 2010: The Parallel Ocean Program (POP) reference manual. Los Alamos National Laboratory Tech. Rep. LAUR-10-01853, 140 pp., https://www.cesm.ucar.edu/models/cesm1.0/pop2/doc/sci/POPRefManual.pdf.

Stommel, H., 1961: Thermohaline convection with two stable regimes of flow. *Tellus*, **13**, 224-230, https://doi.org/10.1111/j.2153-3490.1961.tb00079.x

Suarez, M. J., and P. S. Schopf, 1988: A delayed action oscillator for ENSO. *J. Atmos. Sci.*, **45**, 3283-3287, https://doi.org/10.1175/1520-0469(1988)045<3283:ADAOFE>2.0.CO;2

Sun, D. Z., 1997: El Niño: A coupled response to radiative heating? *Geophys. Res. Lett.*, **24**, 2031-2034, https://doi.org/10.1029/97GL01960

Sutton, R. T., G. D. McCarthy, J. Robson, B. Sinha, A. T. Archibald, and L. J. Gray, 2018: Atlantic multidecadal variability and the U.K. ACSIS program. *Bull. Amer. Meteor. Soc.*, **99**, 415-425, https://doi.org/10.1175/BAMS-D-16-0266.1

Thirumalai, K., T. M. Quinn, Y. Okumura, J. N. Richey, J. W. Partin, R. Z. Poore, and E. Moreno-Chamarro, 2018: Pronounced centennial-scale Atlantic Ocean climate variability correlated with Western Hemisphere hydroclimate. *Nat. Commun.*, **9**, 392, https://doi.org/10.1038/s41467-018-02846-4

Thornalley, D. J. R., and Coauthors, 2013: Long-term variations in Iceland-Scotland overflow strength during the Holocene. *Climate Past*, **9**, 2073-2084, https://doi.org/10.5194/cp-9-2073-2013

Tziperman, E., L. Stone, M. A. Cane, and H. Jarosh, 1994: El Niño chaos: Overlapping of resonances between the seasonal cycle and the Pacific ocean-atmosphere oscillator. *Science*, **264**, 72-74, https://doi.org/10.1126/science.264.5155.72

Vellinga, M., and P. L. Wu, 2004: Low-latitude freshwater influence on centennial variability of the Atlantic thermohaline circulation. *J. Climate*, **17**, 4498-4511, https://doi.org/10.1175/3219.1

Wanner, H., and Coauthors, 2008: Mid- to late Holocene climate change: An overview. *Quat. Sci. Rev.*, **27**, 1791-1828, https://doi.org/10.1016/j.quascirev.2008.06.013

Wei, X., and R. Zhang, 2022: A simple conceptual model for the self-sustained multidecadal AMOC variability. *Geophys. Res. Lett.*, **49**, 11, https://doi.org/10.1029/2022GL099800

Welander, P., 1982: A simple heat-salt oscillator. *Dyn. Atmos. Oceans*, **6**, 233-242, https://doi.org/10.1016/0377-0265(82)90030-6

Wills, R. C., T. Schneider, J. M. Wallace, D. S. Battisti, and D. L. Hartmann, 2018: Disentangling global warming, multidecadal variability, and El Niño in Pacific temperatures. *Geophys. Res. Lett.*, **45**, 2487-2496, https://doi.org/10.1002/2017GL076327

Winton, M., and E. S. Sarachik, 1993: Thermohaline oscillations induced by strong steady salinity forcing of ocean general-circulation models. *J. Phys. Oceanogr.*, **23**, 1389-1410, https://doi.org/10.1175/1520-0485(1993)023<1389:TOIBSS>2.0.CO;2

Yin, F. L., 1995: A mechanistic model of ocean interdecadal thermohaline oscillations. *J. Phys. Oceanogr.*, **25**, 3239-3246, https://doi.org/10.1175/1520-0485(1995)025<3239:AMMOOI>2.0.CO;2

Zhang, R., and Coauthors, 2019: A review of the role of the Atlantic meridional overturning circulation in Atlantic Multidecadal Variability and associated climate impacts. *Rev. Geophys.*, **57**, 316-375, https://doi.org/10.1029/2019RG000644